이학박사학위논문

Optical force enhancement and its application to molecular fractionation

광력의 증강과 광력을 이용한 분자 분리

2016 년 2 월

서울대학교 대학원

화학부 물리화학전공

Sun Xing Nan

광력의 증강과 광력을 이용한 분자 분리

서울대학교 대학원 화학부 물리화학 전공

손성남

초록

광력을 이용하여 분자의 외부 자유도를 조절하는 방법은 많은 연구에 적용되고 있는데 그 예로 분자 집광, 분자 분리, 그리고 분자의 가속과 감속 등이 있다. 분자 광학 실험의 다양성을 높이기 위하여 낮은 파워와 낮은 최대 세기를 가진 레이저를 이용하여 보다 효율적인 분자 조절 방법을 개발하는 것이 필요하다. 분자 조절에 가장 많이 사용되고 있는 쌍극자 광력은 분자의 편극률과 레이저장의 기울기에 비례하게 되어서 레이저장의 기울기를 높여주는 방식으로 쌍극자 광력을 증강시킬 수 있다. 여기서 우리는 좁게 집광된 레이저 빔과 광학적 정상파를 이용하여 레이저장의 기울기를 높여주어 광력을 증강시켰고 이렇게 증강된 광력을 이용하여 분자를 분리하는 방법에 대하여 논한다.

주요어: 비공명 쌍극자 광력, 분자 광학, 유효 편극률, 레이저장의 기울기, 집광, 광학적 정상파.

Optical force enhancement and its application to molecular fractionation

Sun Xing Nan

Physical chemistry, department of chemistry, Seoul National University

Abstract

Controlling molecular external degrees of freedom using optical forces leads to various applications, such as molecule focusing, separation, slowing, and acceleration. Developing a more efficient method, in which lasers of lower powers and intensities are used, is important to enable a variety of experiments. The optical dipole force, which is most widely used for molecule control, is proportional to the molecular polarizability and field gradient and thus can be improved by increasing the field gradient. Efficient deflection of molecules is achieved by employing a tightly focused laser beam or a standing wave composed of two counter-propagating laser beams. We also discuss the application of the enhanced optical force to molecular fractionation with respect to the effective polarizability-to-mass ratios.

Key words: non-resonant dipole force, molecule optics, effective polarizability, field gradient, focusing, standing wave.

Contents

Chapter 1

Background

1.1 Introduction

A photon carries a linear momentum of $\hbar k$, where $\hbar = h/2\pi$ is the Dirac constant and k is the wavevector. When photons are absorbed, reflected, or refracted by an object, the photon momenta are transferred to the object. Thus, the object momentum is changed. The rate of the momentum change is equal to the force exerted by light according to Newton's second law.

A pioneering work on object manipulation using the optical force was reported by Ashkin in 1970. Acceleration and trapping of micron-sized particles using the radiation pressure were achieved [1]. In that paper, Ashkin also proposed that the radiation pressure could be used to control atoms or molecules. Afterwards, a great deal of development in the field of optical manipulation was achieved. In the subject of atomic physics, atomic slowing [2], cooling, trapping [3], and Bose-Einstein condensation [4] of trapped atoms were achieved, for which Nobel Prizes in physics in 1997 and 2001 were awarded. A remarkable development of optical manipulation can be seen not only in atomic physics, but also in other subjects such as molecular physics, chemistry, and chemical biology [5,6].

1.2 Microparticle manipulation using light

Optical manipulation of large particles, where the particle size is larger than laser wavelengths, should be treated using ray optics. Light ray trajectories in a laser beam change when they are scattered by a particle. Since photons in a laser beam carry linear momenta, the photon momentum changes are transferred to the particle, which causes a scattering force. A focused Gaussian beam also applies a force to particle along the gradient of the laser intensity, which causes the trapping of the particle in the laser beam[7]. This trapping method is called optical tweezers.

Similar to the linear momentum, the photon angular momentum of circularly polarized light can also be transferred to particles, exerting torques. Spinning of birefringent material particles after receiving the angular momentum from light was observed [8,9]. The elongated particle alignment, where the longer axis of the particle aligns along the laser polarization direction, has also been reported [8,10]. The principle of micron-sized particle alignment is quite similar to that of small molecule alignment [11], for which the energy of interaction of linearly polarized light with particles depends on the particle orientation with respect to the polarization direction. Many manipulation methods and their applications are shown in a review paper [6].

1.3 Atom manipulation using optical forces

When an atom absorbs a photon of a resonant laser beam, the atom receives a linear momentum of $\hbar k$ from the photon. Since the atom re-emits the photon in a random direction, the net momentum change of the atom is $n\hbar k$ along the laser propagating direction through n-cycles of absorption and emission. These kinds of cycling methods are used for slowing, cooling, and trapping of the atoms with laser beams, which are well described in the literature [2,3]. Red-detuned counter-propagating laser beams in which a rest atom hardly adsorbs are employed in the Doppler cooling of the atom. When an atom moves toward one of the laser beams, the energy gap of the atom becomes resonant with the laser beam. Therefore the atom absorbs and emits the photons until it becomes off-resonant with the laser beam. Consequently, the atom loses its kinetic energy. On the other hand, a Zeeman slower was used to slow down atoms in a molecular beam. An atomic beam traveling in a slowly varying magnetic field from a high to a low field encounters a laser beam of frequency resonant with the atoms in the high magnetic field. The lowering magnetic field permits the slowed-down atoms to stay resonant with the laser beam so that the atoms are slowed down continuously. More techniques about atom manipulations are described in the literature [2,3].

1.4 Molecule manipulation using optical forces

It is difficult to apply the aforementioned optical cycling methods, which are utilized to cool and slow atoms, to molecule manipulation since optical pumping into dark states forces the cycling process to end. Until now, only few special molecules, such as SrF [12-15] and YO [16], have been slowed or cooled through the cycling process using an additional repumping laser [12-15] or microwave mixing [16] to prevent them from falling into dark states. Therefore, the nonresonant optical dipole force, the negative gradient of the Stark interaction energies of lasers far off-resonant with molecules is mostly used to manipulate molecules. Stark interaction energy U of a molecule at its ground state is described by [17-19]:

$$U = -\frac{1}{4}\alpha E^2 = -\frac{1}{2}\alpha \eta I , \tag{1}$$

where α is the molecular polarizability, E is the laser electric field, η is the vacuum impedance, and I is the laser intensity. Equation (1) indicates that a ground state molecule is a high-field seeker since the molecule is forced to move towards the high-field region of laser beams of lower Stark energy. An examples is an inhomogeneous laser field of a focused Gaussian beam used for deflecting [17], focusing [20], separating [21], or slowing [22] molecules.

Since the optical dipole force is proportional to the field gradient, it can be enhanced by increasing the field gradient. Methods such as tight focusing of a Gaussian laser beam [23], employing a standing wave composed of two coherent laser beams [24], or using surface plasmon fields [25] can be used to increase the field gradient.

1.5 Effective polarizability

The molecular polarizability is a tenser described as:

$$\alpha = \begin{pmatrix} \alpha_{xx} & 0 & 0 \\ 0 & \alpha_{yy} & 0 \\ 0 & 0 & \alpha_{zz} \end{pmatrix}, \tag{2}$$

where α_{xx}, α_{yy}, and α_{zz} are the polarizabilities along the molecular axes *x*, *y*, and *z* in the molecular frame, respectively. For a linear or symmetric-top molecule, α_{xx} can be written as $\alpha_{\parallel}$, and α_{yy} as well as α_{zz} can be written as $\alpha_{\perp}$, where $\alpha_{\parallel}$ and $\alpha_{\perp}$ denotes the molecular polarizabilities parallel and perpendicular to the molecular axis, respectively.

When a linear molecule is placed in a linearly polarized laser field (see Figure 1), the instantaneous induced dipole moment is [18]

$$\mu_{ind} = (\alpha_{\parallel} \cos^2\theta + \alpha_{\perp} \sin^2\theta)E = (\alpha_{\Delta} \cos^2\theta + \alpha_{\perp})E\,, \tag{3}$$

where α_{Δ} is $\alpha_{\parallel} - \alpha_{\perp}$, and θ is the instantaneous angle between the molecular axis and the direction of the laser polarization. Thus, the instantaneous effective polarizability of the molecule is $\alpha_{\Delta} \cos^2\theta + \alpha_{\perp}$. However, the molecule rotates in time; hence, the effective polarizability of the molecule must be obtained by averaging the instantaneous effective polarizabilities over time. The result is $\alpha_{\Delta} \overline{\cos^2\theta} + \alpha_{\perp}$. We denote the quantity $\overline{\cos^2\theta}$ of a molecule in the $|J, M\rangle$ rotational state as A_{JM}.

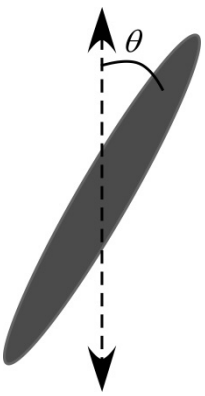

Figure 1. A linear or symmetric-top molecule is placed in the linearly polarized laser field. The instantaneous angle between the molecular axis and the laser polarization direction is θ.

For thermal molecules in a laser field, in which the rotational motion is not perturbed significantly by the laser field, A_{JM} is expressed by [26]:

$$A_{JM} = \left\langle J, M \left| \cos^2 \theta \right| J, M \right\rangle = \frac{1}{3} + \frac{2}{3} \frac{J(J+1) - 3M^2}{(2J+3)(2J-1)}. \quad (4)$$

The distribution function $f(A_{JM})$ of thermal linear molecules has a unimodal rainbow singularity at a maximal value of 1/2 [26,27]. For nonlinear molecules, $f(A)$ is much more complicated owing to the additional rotational quantum number K. A classical approach was introduced in the literature [28].

Aligned pendular states of molecules can be formed in an intense laser field, by anisotropic interaction of the electric field of the laser with the induced dipole moment represented in Eq. (3) [11,18]. The effective polarizabilities can be modified by the alignment effect of molecules in an intense laser field. An approximately 20% different optical dipole force on CS_2 molecules was observed after changing the polarization of the laser beam from linear to circular owing to different alignment effects of molecules in different polarization states [29].

Chapter 2

Efficient nonresonant dipole force on molecules by a tightly focused laser

Abstract

When a molecule is placed in a nonresonant laser field, the Stark interactions between the laser field and the induced molecular dipole result in a mechanical force on the molecule. This nonresonant dipole force is proportional to the intensity gradient of the laser, thus requiring a strong and focused pulsed laser for a sizable impact on the molecule. 36.4 mJ pulses of a 1064 nm Nd:YAG laser focused with a 17.5 cm focal length convex lens produced a 6.4 m/s change in the transverse velocity of a CS_2 molecular beam. Using spherical mirrors with shorter focal lengths such as 10.0, 7.5, and 5.0 cm, dipole forces of similar magnitude were obtained with laser pulses of much lower energies. In particular the 5.0 cm focal length spherical mirror provided an 11.3 m/s change in the transverse velocity using 3.6 mJ laser pulses. This corresponds to 18-fold increase in the deflection efficiency, the ratio between the maximum velocity change and the pulse energy. From the improved efficiency, the nonresonant dipole force can be exerted with ease.

Key words: nonresonant dipole force, carbon disulfide, focusing, deflection, molecule optics

[1]

[1] Based on: Frontiers in Physics 2, 34 (1)

2.1 Introduction

Molecule optics that controls the molecular external degrees of freedom using optical forces from light-matter interactions has grown into a major branch of physics [30,31]. Most widely used optical force is the dipole force—mechanical force of light resulting from molecular induced dipole-light field interactions. Due to the small magnitudes of induced dipoles, focused beams of high energy nonresonant infrared (IR) pulsed lasers have been used to exert a nonresonant dipole force to a molecule. Some examples include a molecule lens focusing a molecular beam [17,20,29], a molecule prism spatially separating a molecular mixture beam [21], a moving periodic optical potential slowing down or accelerating molecules [32-34], and correlated rotational alignment spectroscopy with aligning molecules non-adiabatically [35]. Ideas such as deflection of pre-aligned molecules were also proposed [26,27].

One practical difficulty in molecule optics is the use of a high energy laser which causes issues with molecular ionization and optical component damages. We solved these problems by tight focusing of a laser exerting dipole forces. The dipole force on a molecule is proportional to the gradient of the optical field intensity. In comparison, the direct ionization probability by n photons is proportional to the n-th power of the intensity. Thus, if a lower energy laser is focused more tightly to obtain a dipole force of a similar magnitude, the molecular ionization is significantly reduced, in addition to the laser handling ease. When an IR laser is used for a nonresonant dipole force, more photons are needed than in the case of a visible laser to ionize a molecule. Therefore, the advantage of tight focusing will be more pronounced. Using focusing units of different focal lengths, pulses from a 1064 nm Nd:YAG laser were focused on a CS_2 molecular beam to compare the nonresonant dipole force efficiency. By focusing with a 5.0 cm focal length

spherical mirror, 3.6 mJ pulses produced an 11.3 m/s change in the transverse velocity of the molecular beam. Meanwhile a velocity change of 6.4 m/s was obtained by focusing 36.4 mJ pluses with a 17.5 cm focal length convex lens. The deflection efficiency, given as the ratio of the maximum velocity change and the pulse energy, was improved 18 times greater with a tighter focusing of the IR laser.

2.2 Materials and methods

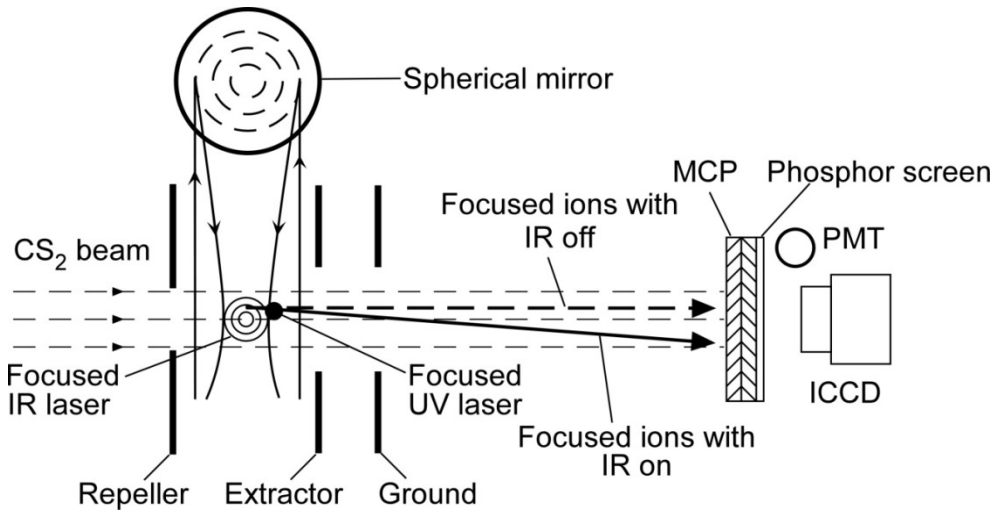

Figure 1. Schematic of the experimental layout. The molecular beam propagates along the *z*-axis while the laser beam is along the *x*-axis. The molecular beam is deflected by an IR laser pulse along the *y*-axis and then ionized by a UV laser pulse.

The experimental setup was similar to the one used by Zhao et al. [21,36]. CS_2 vapor at room temperature was mixed with Ar to 2 atm and expanded to a vacuum system through a pulsed valve at 10 Hz (9-365-900 Solenoid Valve, Parker Instrumentation, Fairfield, NJ, USA). The vacuum system consisted of source and detection chambers, separated by a skimmer (Beam Dynamics, Minneapolis, MN,

USA) with a 0.51 mm diameter hole. The source chamber was pumped by a 2400 L/s diffusion pump (VHS-6, Varian, San Francisco, CA, USA) and a rotary backing pump, yielding a 1.1×10^{-6} Torr pressure. Fig. 1 shows the detection chamber that had a 20 cm cube with a 2.25 inch window for a laser beam to enter the chamber. There was also a 40 cm time of flight (TOF) tube with a 2D-imaging detector at its end. The 2D-imaging detector was a chevron-type microchannel plate (MCP, 3040-FM, Galileo, Sturbridge, MA, USA) and a P47 phosphor screen. The pressure inside the detection chamber was approximately 6×10^{-7} Torr, maintained by pumping with a 250 L/s turbo molecular pump (Turbo-V 250, Varian) and a rotary backing pump.

The expanded gas was collimated by the skimmer to create a molecular beam going through a 0.6 mm pin-hole. The molecular beam was then deflected by a focused IR (wavelength λ = 1064 nm) pulse (10 ns) of a linearly polarized Nd:YAG laser (Powerlite 8000, Continuum, Santa Clara, CA, USA). A Glan-laser polarizer and a half wave plate controlled the polarization direction and IR laser intensity. After a 30 ns delay, the deflected molecular beam was crossed by a focused ultraviolet (UV, λ = 355 nm) pulse (10 ns) of another Nd:YAG laser (Surelite Ⅱ-10, Continuum). The temporal profiles of both IR and UV laser beams were recorded by a photodiode. The UV laser ionized molecules through multiphoton-ionization processes [37]. The focusing degrees were changed by using different focusing components. A 17.5 cm focal length convex lens was placed in front of the detection chamber window to focus the IR and UV lasers. For tighter focusing, spherical mirrors of 5.0, 7.5, and 10.0 cm focal lengths were placed inside the chamber using a triple axis feed-through (PSM-1502, MDC, Hayward, California, USA). We controlled the input laser energy before passing through the focusing units by a half wave plate and a linear polarizer. The IR laser focus center, laser propagation direction, and molecular beam axis were chosen as the origin, *x*-axis, and *z*-axis, respectively.

There was an electrostatic lens system of three electrode plates: a repeller, extractor and ground in the detection chamber. The electrostatic lens system details were provided in our previous report [36]. When the ions were focused onto the MCP by using a combination of three electrodes without grids, ions of the same velocity were mapped onto the same position regardless of their initial positions. This focusing electrode configuration performed velocity map imaging (VMI) [38] detecting the changes in molecular velocities deflected by the nonresonant dipole force by the IR laser pulse. The focal length of the electrostatic lens was controlled by the ratio of the extractor voltage and repeller voltage. The VMI condition in this report was 900, 600, and 0 V for the repeller, extractor, and ground, respectively. The accelerated ions arrived at the 2D detector 13.9 μs after ionization. When the focused molecular ions hit the MCP, the ion signals were amplified and electrons were emitted from its back. The emerged electrons impinged on the phosphor screen, which led to the phosphor screen flash. An intensified CCD camera (ICCD, DH534-18F-04, Andor, Belfast, UK) recorded the images on the phosphor screen. A photomultiplier tube (PMT; 1P21/E717-21, Hamamatsu, Hamamatsu City, Japan) and an oscilloscope (LT344, LeCroy, Seoul, Korea) were also used to measure the TOF of the focused molecular ions.

We scanned the UV laser focus in the *y*-axis by tilting the reflection mirror by 0.5 μm or 1 μm division. In our experimental setup, tilting the reflection mirror 1 μm resulted in 0.76 μm, 1.13 μm, 1.53 μm, and 2.31 μm movement of the UV laser focus for the 5.0 cm, 7.5 cm, 10.0 cm, and 17.5 cm focusing units, respectively. 1500 shot images were averaged, 60 pixels along the *x*-axis near the *x*-center were binned, and the profile was fit to a Gaussian function to obtain the *y*-center at each of the UV laser's *y*-position.

2.3 Results and discussion

The velocity shift of the molecules of mass m in the y-direction by the dipole force is then given by [36,39,40]

$$\Delta v_y = \frac{\Delta Y}{\mathrm{TOF}} = -\frac{\sqrt{2\pi}\alpha\eta I_0 y}{m\omega_0 v_z \sqrt{1+2(\ln 2)(\omega_0/v_z\tau)^2}} \exp\left(-\frac{2y^2}{\omega_0^2}\right), \qquad (1)$$

where ΔY is the distance between the y-centers of ion images obtained with the IR laser turned on and off. TOF is time of flight of the deflected ions. The y value is the y-coordinate of the UV laser focus with respect to that of the IR laser at the origin. Alpha is molecular polarizability, η is the impedance of vacuum. I_0, ω_0, and τ are the peak intensity, beam waist radius, and pulse duration (full width at half maximum), respectively.

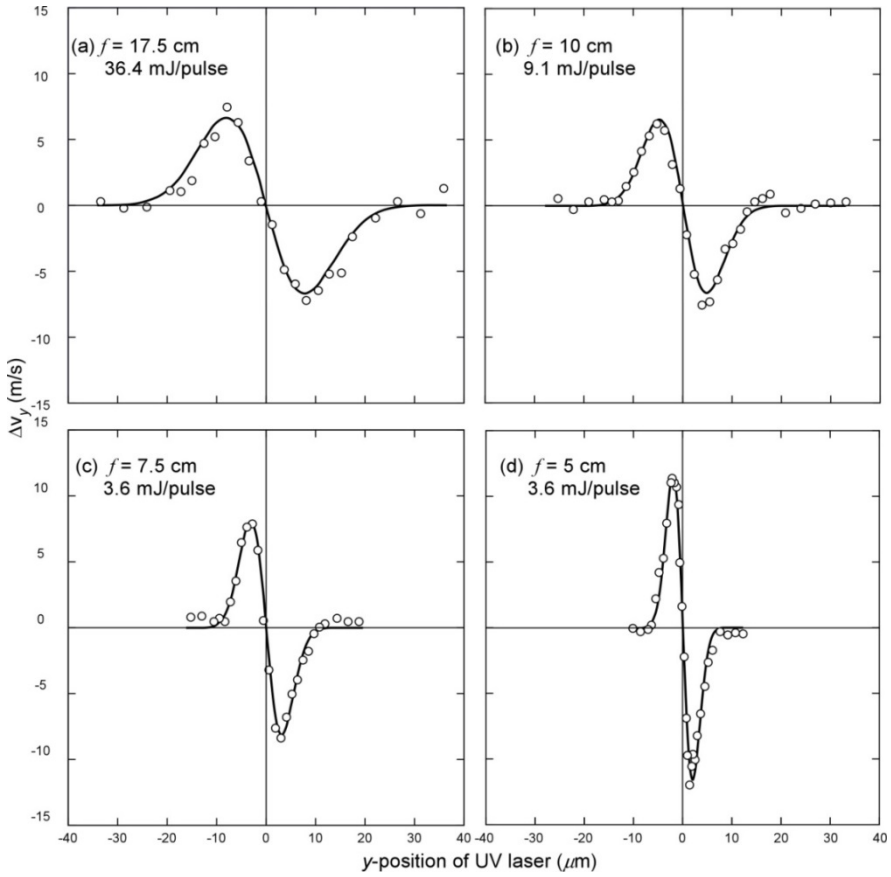

Figure 2. Deflection curves of the transverse velocity change along the *y*-axis versus the relative *y*-position. (a) Focusing the IR laser with a 17.5 cm focal length lens for 36.4 mJ/pulse, $I_0 = 0.65 \times 10^{12}$ W/cm^2. (b) Focusing the IR laser with a 10.0 cm focal length mirror for 9.1 mJ/pulse. $I_0 = 0.47 \times 10^{12}$ W/cm^2. (c) Focusing the IR laser with a 7.5 cm focal length mirror for 3.6 mJ/pulse. $I_0 = 0.43 \times 10^{12}$ W/cm^2. (d) Focusing the IR laser with a 5.0 cm focal length lens for 3.6 mJ/pulse. $I_0 = 1.09 \times 10^{12}$ W/cm^2. The circles are the measured velocity changes along the *y*-axis and the solid lines are fits to Eq. (1).

To investigate the effects of the nonresonant dipole force by the IR laser pulse on the molecular beam, the experimentally obtained Δv_y values (= ΔY/TOF) were compared with the theoretical predictions provided in Eq. (1). The beam waist radius (ω_0) was determined by fitting the results to Eq. (1). Fig. 2a shows that 36.4 mJ/pulse IR laser pulses focused with the 17.5 cm focal length convex lens produced Δv_{max} = 6.7 m/s at $y = \pm \omega_0/2$ with ω_0 = 15.7 μm. When the spherical mirror of 10.0 cm focal length inside the detection chamber was used, 9.1 mJ IR pulses produced Δv_{max} = 6.6 m/s and ω_0 = 9.5 μm (Fig. 2b). Thus the tightly focused laser pulses of one-quarter energy exerted nonresonant dipole forces of similar magnitudes on CS_2 molecules. Furthermore, with the 7.5 cm focal length spherical mirror, laser pulses with only one-tenth energy of 3.6 mJ/pulse produced Δv_{max} = 6.3 m/s and ω_0 = 8.1 μm (Fig. 2c). When the 5.0 cm focal length spherical mirror was used for 3.6 mJ/pulse IR laser pulses, a tighter focusing yielded Δv_{max} = 11.6 m/s and ω_0 = 4.0 μm (Fig. 2d). The average ω_0 and Δv_{max} values are listed in Table 1. At 10 mJ/pulse or lower energy levels, the complications from molecular ionization and optical component damages were practically non-existing.

In a Gaussian-beam optical system, the beam waist radius is given by [41]

$$\omega_0 = \frac{\lambda M^2}{\pi \omega_L} f \,, \tag{2}$$

where f is the focal length of the focusing mirror (or lens) and ω_L is the radius of the collimated beam at the mirror (or lens). The $1/e^2$ width of the IR laser beam equal to $2\omega_L$ was 9.6 mm. M^2 is the quality factor (1.0 for an ideal Gaussian beam). Fig. 3 is a plot of ω_0 *vs. f*. The circles are the data from the deflection curves using Eq. (1) and the solid line represents Eq. (2) with $M^2 = 1$. Our data shows that the focused spot size was proportional to the focal length of the focusing unit with $M^2 = 1.5$ as shown with a dotted line.

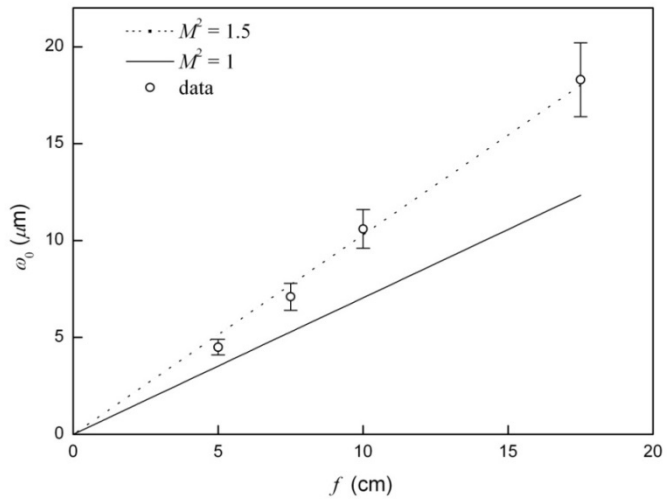

Figure 3. The relationship between the beam waist radius and focal length. The measured data are denoted by the circles. The solid line is a plot of Eq. (2) with $M^2 = 1$ and the dotted line with $M^2 = 1.5$.

Using the energy per pulse G of a Gaussian profile, the deflection

efficiency defined as $\Delta v_{max}/G$ becomes

$$\frac{\Delta v_{max}}{G} = \frac{2\sqrt{2\ln 2}\alpha\eta}{\pi\sqrt{e}\omega_0^2 m v_z \tau\sqrt{1+(2\ln 2)\left[\omega_0/(v_z\tau)\right]^2}}. \quad (3)$$

Fig. 4 is a plot of the deflection efficiency as a function of ω_0. When the focal length of the focusing unit was reduced, the deflection efficiency increased to 0.18 × 10^3 (f = 17.5 cm), 0.72 × 10^3 (f = 10.0 cm), 2.0 × 10^3 (f = 7.5 cm), and 3.1 × 10^3 (f = 5.0 cm) m s^{-1} J^{-1}. Therefore, the deflection efficiency was enhanced more than 18-fold with tighter focusing using the 5.0 cm spherical mirror compared to the 17.5 cm convex lens. The results are listed in Table 1. The solid line represents the theoretical deflection efficiency of Eq. (3) using α = 9.7 × 10^{-40} C m^2 V^{-1}, η = 376.7 Ω, v_z = 498 m/s [42], m = 1.26 × 10^{-25} kg, and τ = 10 ns. The experimental data provided with error bars showed a similar pattern with the theoretical line, but it deviates from the theoretical line with respect to the ω_0 reduces. The deflection efficiency which was reported in reference [17] is about 1.2 × 10^3 m s^{-1} J^{-1}, however, the laser pulse duration and the molecular beam velocity in this experiment is different from ours. So, in order to compare our data with the results in the reference [17], Fig. 4 also showed the data and theoretical prediction with the experimental condition in reference [17].

Table 1. Molecular deflection with tight focusing

f	ω_0	G	Δv_{max}	$\Delta v_{max}/G$
(cm)	(μm)	(10^{-3} J)	(m/s)	(×10^3 m s^{-1} J^{-1})
5.0	4.5 ± 0.4	3.6	11.3 ± 0.5	3.1 ± 0.14
7.5	7.1 ± 0.7	3.6	7.9 ± 0.6	2.0 ± 0.18
10.0	10.6 ± 1.0	9.1	6.4 ± 0.3	0.72 ± 0.04
17.5	18.3 ± 1.9	36.4	6.4 ± 0.3	0.18 ± 0.01

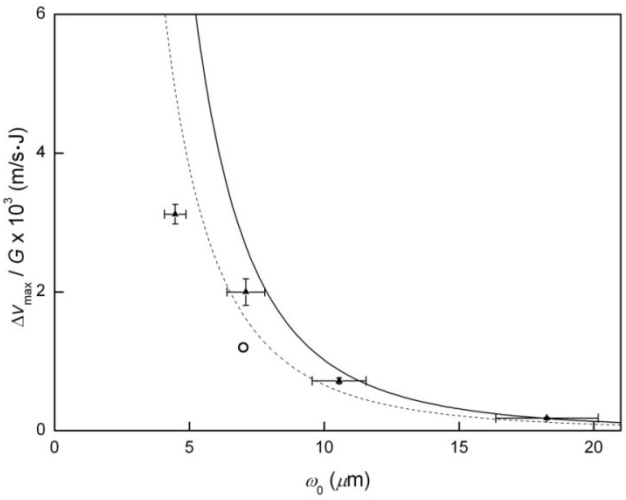

Figure 4. $\Delta v_{max}/G$ versus ω_0. The solid line represents the deflection efficiency in Eq. (3). The filled triangles are the experimental data showing a similar pattern. The dashed line is deflection efficiency with the experimental conditions in Ref. [17], and the circle is the result in Ref. [17].

2.4 Conclusions

Using a short focal length mirror, we demonstrated that a low power laser pulse could exert a nonresonant dipole force on the molecule to yield a sizable impact on the molecular motion. The gradient of the focused laser intensity was increased to result in a larger dipole force with a shorter focal length. 1/10 energy IR laser pulses focused by a 5.0 cm mirror produced a 1.8-fold change in the transverse velocity of a CS_2 molecular beam compared to the case with a 17.5 cm lens. The deflection efficiency was enhanced 18-fold. Therefore, the nonresonant dipole can be utilized for molecule optics with much less concern for problems such

as ionization, fragmentation of molecules, or optical component damages. Day to now, only high energy pulse laser at fixed wavelengths was used in the molecular deflection experiment. Since a pulse energy of 5 mJ can be provided easily by a tunable dye laser over visible and near IR ranges, it can be investigated how the wavelength variation of the deflection laser affects the molecular deflection.

Chapter 3

Rotational state-dependent dispersion of molecules by pulsed optical standing waves

Abstract

We report on the rotational state-dependent, transverse acceleration of CS_2 molecules affected by pulsed optical standing waves. The steep gradient of the standing wave potential imparts far stronger dipole forces on the molecules than propagating pulses do. Moreover, large changes in the transverse velocities (i.e., up to 80 m/s) obtained with the standing waves are well reproduced in numerical simulations using the effective polarizability that depends on the molecular rotational states. Our analysis based on the rotational state-dependent effective polarizability can therefore serve as a basis for developing a new technique of state selection for both polar and nonpolar molecules.

[2]

[2] Based on: Physical Review Letters 115, 223001

3.1 Introduction

During the last two decades, optical manipulation of molecules has been an important subject in many experimental and theoretical studies. A nonresonant laser field exerts a dipole force on molecules proportional to the molecular polarizability. Propagating nonresonant laser fields have been used to control the angular, transverse, and longitudinal motions of molecules. Strong laser pulses also have been used to align molecules [11,18]. A combination with an electrostatic field produces an orientation of polar molecules [43-48]. Focusing a molecular beam [49] and separating a molecular mixture beam [50] were proposed, and a molecule lens [17,20,36] and a molecule prism [21] have been realized. It was also suggested that molecules could be decelerated using a nonresonant laser field [22,51]. Coupling between the angular and the translational motions enabled the adjustments of the deceleration by aligning the molecules with the laser field [29,52]. In addition, efficient control of molecular deflection by preshaping the angular distribution was discussed [26,27].

On the other hand, the standing wave potential, formed by two counter-propagating lasers, has been employed to control the forward velocity of molecules. An atom and molecule mirror made of a pulsed standing wave was suggested [53]. An accelerator [54] and a decelerator [55] for atoms and molecules using pulsed traveling standing waves with increasing and decreasing velocities, respectively, were discussed. Furthermore, the possibility of slowing down and bunching molecules by means of a traveling potential with a constant velocity was studied [56]. These theoretical studies were followed by experimental realizations. A pulsed standing wave changed the velocity distribution of hydrogen molecules by 200 m/s [57]. Traveling potentials with constant velocities were used to decrease the velocity of NO molecules [58] and to prepare stationary benzene molecules [33]. Recently, the velocity of metastable argon atoms initially trapped in a magneto-optical trap was accelerated by an accelerating periodic potential [34].

The angular motions of molecules determine their effective polarizabilities,

which in turn affect their translational motions in a manner dependent on the rotational states. Thus the interaction between molecules and laser fields was recognized to be rotational state-dependent [11,18,26-28,44,49,50,59,60], and the possibility of separating quantum states with laser fields was discussed in theoretical studies [26-28,50,59-61]. However, almost all the experimental results [11,17,20,21,29,33,36,58] were analyzed using a single polarizability value averaged over all quantum states.

Here we report on the transverse dispersion of a CS_2 molecular beam by pulsed optical standing waves and its interpretation in terms of the rotational state-dependent molecular polarizability. The velocity spread of the dispersed molecules is about 160 m/s, which is too large to be accounted for solely by using the average polarizability. For this reason, we use the rotational state-dependent polarizability to simulate the velocity spreads, which are in excellent agreement with the experimental results. In this way, we demonstrate the dependence of the dipole force on the rotational states, and show its importance in understanding molecular transverse motions affected by optical standing waves. Our report therefore serves as a cornerstone for developing a new state-selection technique that is potentially applicable to both polar and nonpolar molecules. The control over the molecular transverse motion is complementary to the deceleration and acceleration of molecules [33,34,57,58].

3.2 Experimental

A schematic of the experimental setup is shown in Fig. 1. The apparatus operates at 10 Hz. We define the *y*- and *z*- axes as the vertical and the molecular beam directions, respectively. The infrared laser (IR1) propagates parallel to the positive *x*-axis. The coordinate origin is at the IR1 focus, which overlaps with the IR2 focus. The molecular beam is formed by seeding 0.3 vol% CS_2 vapor in Ar gas

and expanding the mixture, held at a pressure of 2 atm, through a pulsed valve of a nozzle into a vacuum chamber. With similar source conditions, the rotational temperature T was estimated to be 35 K in the previous report [29]. After passing through a skimmer, the molecular beam enters a second chamber at 1×10^{-7} Torr. The molecular beam is then collimated by a pinhole. At 8.5 cm downstream from the nozzle, the molecular beam is crossed by a pulsed standing wave potential.

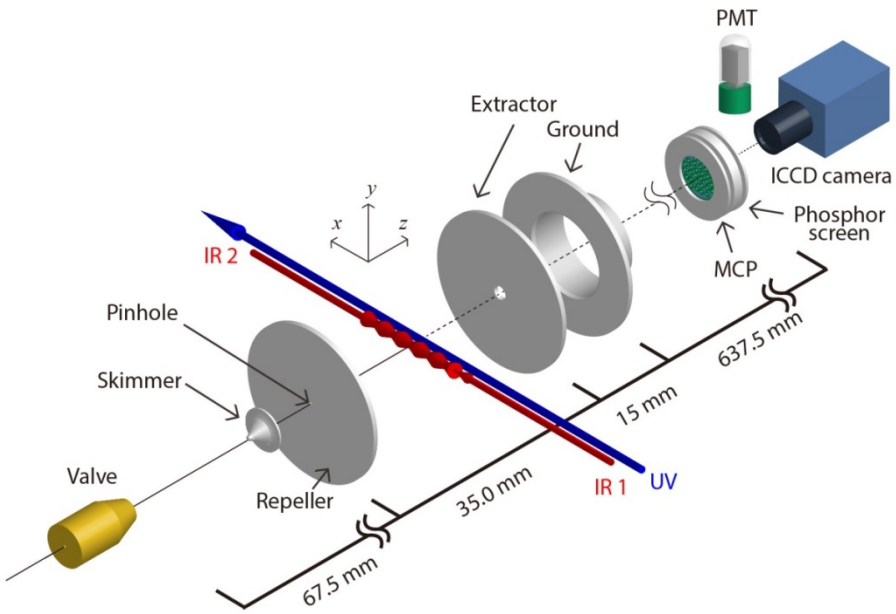

FIG. 1. Schematics of the experimental setup.

The pulsed standing wave is created by overlapping two counter-propagating pulses (IR1 and IR2) with the same peak intensity I_0 at the center of the second chamber. Their pulse width and wavelength are τ = 12.5 ns (FWHM) and λ = 1064 nm, respectively. The two pulses are formed by splitting a single pulse from

an injection-seeded Nd:YAG laser. After splitting, the energy and polarization of the two pulses are adjusted by two sets of a zero-order half-wave plate and a Glan-Laser polarizer, respectively. Then the two pulses, which are linearly polarized along the *y*-axis, are focused by two lenses with focal lengths of 20 cm into the second chamber. The waist radius ω_0 of the pulses is 21 μm.

After a delay of 30 ns, the molecular beam, which has interacted with the pulsed standing wave potential, intersects with an lineraly polarized ultraviolet (UV) probe laser pulse which is a third-harmonic of another Nd:YAG laser with τ = 7.1 ns and λ = 355 nm. The lens in front of the second chamber also focuses the UV pulse. Considering the delay of 30 ns, the UV laser focus is also spatially shifted along the *z*-axis to ionize only the dispersed molecules through multiphoton ionization processes.

The dispersed and subsequently ionized molecules are accelerated and focused by an electrostatic lens system onto a microchannel plate (MCP) after flying 67 cm through a time-of-flight (TOF) tube. The system consists of three electrodes; a repeller, an extractor, and a ground. The voltages of the repeller and the extractor are set to 900 and 600 V, respectively, which provides the velocity map imaging condition [38]. In this way, the transverse velocity of an ion is measured from the ratio between its position at the detector and the TOF. The ion signals are converted into luminescence by an MCP and a phosphor screen, which is simultaneously detected by a photomultiplier tube (PMT) and an intensified charge-coupled device (ICCD) camera. The TOF spectrum from the PMT is used to gate the ICCD camera to record images of a selected ion species.

3.3 Results and discussion

Figure 2a shows a velocity map image of CS_2 molecular ions without IR1 or IR2. When only IR1 of low intensity is applied to the molecular beam, it hardly affects the molecular velocity distribution. Fig. 2b shows an ion image with IR1 of

I_0 = 4.9 × 10^{10} W/cm^2, almost identical to Fig. 2a obtained without any IR pulses. Since the intensity of the UV pulse of 0.8 × 10^{10} W/cm^2 is five times smaller than that of IR1, we can ignore the effect of the UV pulse on the velocity distribution. However, when a pulsed standing wave is formed by IR1 and IR2 with their intensities set to 4.9 × 10^{10} W/cm^2 each, a drastic change takes place, as shown in Fig. 2c. $|v_x|$ increases to about 60 m/s, whereas v_y is affected little.

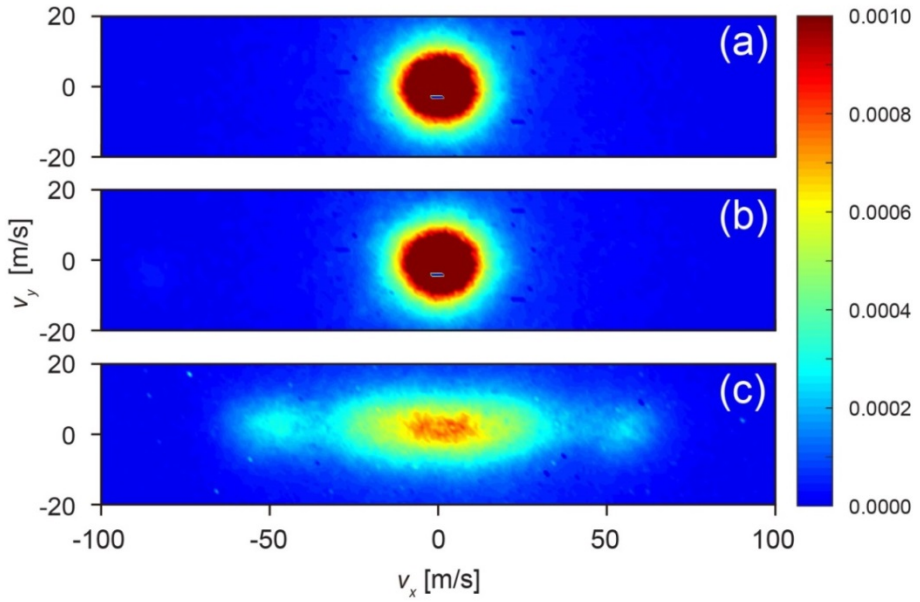

FIG. 2. The velocity map ion images of CS_2 molecules (a) without any IR laser, (b) with IR1 of I_0 = 4.9 × 10^{10} W/cm^2, and (c) with the pulsed optical standing wave made of IR1 and IR2 of I_0 = 4.9 × 10^{10} W/cm^2. The color bar in the image denotes the fraction of the molecules.

The rotational state-dependent molecular polarizability is the key to

understanding the structures shown in the velocity distribution in Fig. 2c. The interaction potential between the standing wave field with wavelength λ and waist radius ω_0 and a molecule with an effective molecular polarizability α_{eff} at time t is given by:

$$U(x, y, z, t) = -2\alpha_{\text{eff}}\eta_0 I_0 \exp[-2(y^2+z^2)/\omega_0^2]\exp[-4(\ln 2)t^2/\tau^2]\cos^2(2\pi x/\lambda), \quad (1)$$

with the vacuum impedance η_0. The first and second exponential terms represent the spatial and temporal profiles, respectively, whereas the $\cos^2(2\pi x/\lambda)$ term corresponds to its periodic variation along the x-axis. The force on the molecule $\mathbf{F}(x, y, z, t) = -\nabla U(x, y, z, t)$ along the x- and y-axes is characterized by the inverse of λ and ω_0, respectively. Therefore, the maximum accelerations along the x- and y-axes differ by a factor of 20.

A linear molecule such as CS_2 has an anisotropic polarizability, whose components parallel and perpendicular to the molecular axis are $\alpha_{\parallel}$ and $\alpha_{\perp}$, respectively. When a linear molecule is oriented at a polar angle θ with respect to the laser polarization axis, the effective polarizability is given by $\alpha_{\text{eff}} = (\alpha_{\parallel} - \alpha_{\perp})\ \overline{\cos^2\theta}\ + \alpha_{\perp}$. For a rotational state $|J, M\rangle$:

$$\overline{\cos^2\theta} = \langle J, M | \cos^2\theta | J, M \rangle = \frac{1}{3} + \frac{2}{3}\frac{J(J+1) - 3M^2}{(2J+3)(2J-1)}. \quad (2)$$

Therefore, the effective polarizability varies with J and M, the quantum numbers associated with the angular momentum and its projection on the laser polarization axis, respectively. At a rotational temperature of T = 35 K, the value of $\alpha_{\text{eff}}(J, M)$ for CS_2 ($\alpha_{\parallel} = 16.8 \times 10^{-40}$ C m^2 V^{-1} and $\alpha_{\perp} = 6.2 \times 10^{-40}$ C m^2 V^{-1} [62]) varies from 6.2 to 12.6 $\times$ 10^{-40} C m^2 V^{-1} with an average of 9.7 $\times$ 10^{-40} C m^2 V^{-1}. On the other hand, at very low rotational temperatures, a few states of low J are populated, whose effective polarizabilities are rather discrete. For example, $\alpha_{\text{eff}}(2, M)$ = 11.8, 10.7, and 7.7 $\times$ 10^{-40} C m^2 V^{-1} for $|M|$ = 0, 1, and 2, respectively. Thus, each state is affected quite differently, which can in principle be exploited to separate the

different rotational states.

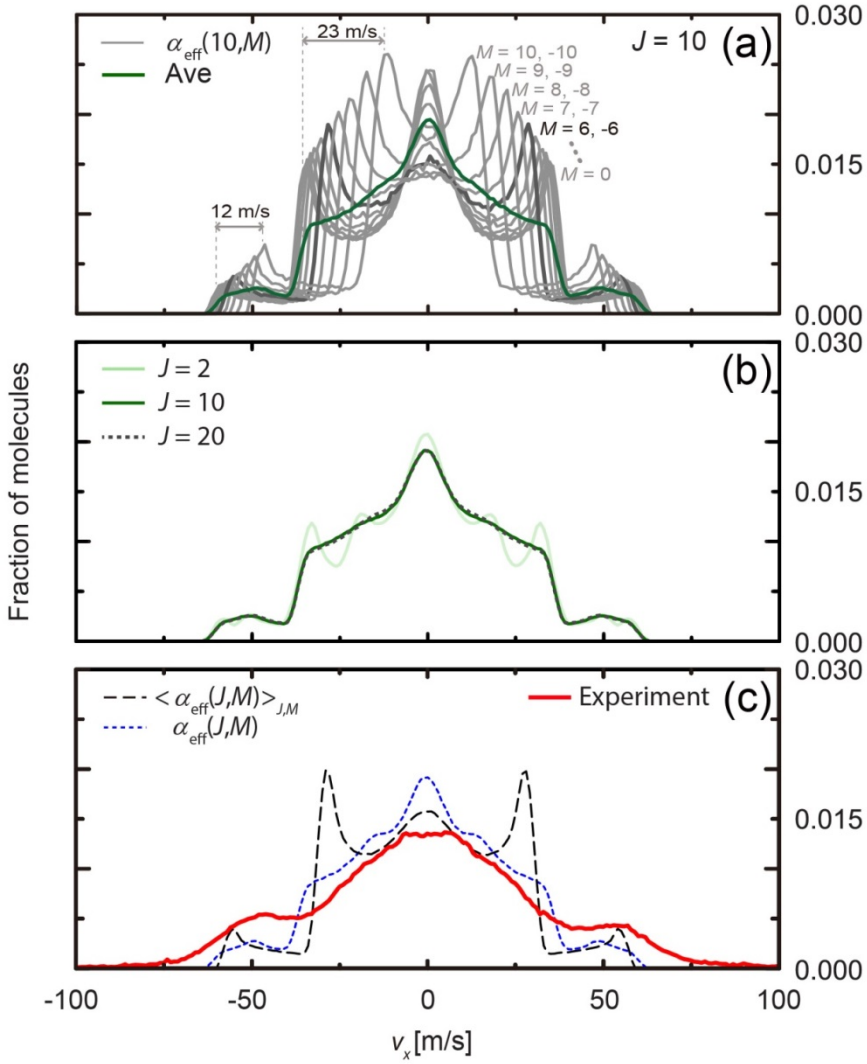

FIG. 3. (a) Simulated velocity profiles for 21 rotational states of J = 10 (gray lines) and their average (dark green solid line). (b) Similar summation profiles for J = 2, 10, and 20. (c) Comparison of the velocity profile of Fig. 2c (red line) with those calculated by using state-dependent ($\alpha_{eff}(J, M)$; blue dotted line) and state-

independent polarizabilities ($<\alpha_{\mathrm{eff}}(J, M)>_{J,M}$; black dashed line).

Figure 3 shows how the rotational state-dependent polarizability contributes to the velocity distribution of Fig. 2c. Considering the negligible effect of the standing wave on v_y as shown in Fig. 2, instead of the two-dimensional velocity distribution function for molecules dispersed by the standing wave, $g(v_x, v_y)$, we use its profile $h(v_x)$ along the v_x-axis; in other words, the binning of $g(v_x, v_y)$ along the v_y-axis. The velocity change that results from the dipole force of **F** on a molecule of mass m is given by:

$$\Delta v_i = \int \frac{1}{m} F_i(x, y, z, t) dt \qquad (i = x, y, z,),$$

which is solved numerically. Since $U(x, y, z, t)$ is proportional to α_{eff}, which is a function of J and M, the force on the molecule depends on the molecular rotational state, and so does the velocity change. Here, we assume that the CS_2 molecules are not aligned by the laser field, since the alignment effect of CS_2 molecules is negligible at field intensities below 1.0×10^{11} W/cm^2 [63]. Trajectory calculations of 9×10^6 molecules yield the velocity distribution $g(v_x, v_y)$. The initial velocity (v_{0x}, v_{0y}, v_{0z}), initial position (x_0, y_0, z_0), and rotational state of an individual molecule are sampled by the Monte Carlo method. The initial transverse velocity distribution is approximated by a two-dimensional Gaussian function with FWHMs of $\Delta v_x^{\mathrm{init}} = 7.2$ and $\Delta v_y^{\mathrm{init}} = 3.4$ m/s, which are given by line-of-sight arguments [17]. The asymmetric spreads result from the ionization volume being elongated along the x-axis. A Gaussian distribution with the most probable velocity v_{mp} of 560 m/s [64] and FWHM of 56 m/s is used as a probability function for v_{0z}. Here, we assume that the FWHM is 10% of the most probable velocity [57,65]. x_0 and y_0 are chosen randomly from a 600 μm × 3 μm rectangle. The range of the distribution is approximate to the ionization range. We ignore the beam divergence and consider

the multiphoton ionization process involving three photons.

On the other hand, z_0 is determined from v_{0z} such that the individual molecule arrives at the plane $z = v_{mp}t_{delay}$ at $t = t_{delay}$. Therefore, $z_0 = v_{mp}t_{delay} - v_{0z}t_{simul}$, where t_{delay} and t_{simul} are the delay between the two IRs and the probe laser beam and the total simulation time, respectively. The molecule occupies a certain $|J, M>$ state with a probability P_J of $e^{-BJ(J+1)/kT}/q_r$, where B, k, and q_r are the rotational constant of the molecule, Boltzmann constant, and rotational partition function, respectively. J is restricted to even numbers because of the zero nuclear spin of ^{32}S [66]. The trajectory calculation includes a thermal distribution of molecules over rotational states at T = 35 K, which was estimated in the previous report [29]. It is worth noting that a temperature change of ±10 K hardly affects the simulation results. Here, we use ω_0 = 23.5 μm and τ = 10 ns, which are within the error ranges of the measured values of ω_0 = 21.5 ± 2 μm and τ = 12.5 ± 2 ns, respectively.

In Fig. 3a, 21 profiles of $h(v_x; J = 10, M)$ are drawn in gray lines, assuming that all the molecules occupy each $|J = 10, M>$ state. Since $h(v_x; J = 10, M) = h(v_x; J = 10, -M)$, they are overlapped in Fig. 3a and the total number of the profiles is 21. In each profile, there are strong rainbow-like singularities associated with the existence of the maxima (minima) in the deflecting standing wave [67], whose positions move outward as $|M|$ decreases – i.e., as α_{eff} increases. As $\alpha_{eff}(10, |M|)$ ranges from 6.7 (M = 10) to 11.5 ($|M|$ = 0) × 10^{-40} C m^2 V^{-1}, the positions of the inner and the outer singularities span from ±12 to ±35 m/s and from ±46 to ±58 m/s, respectively. The congestions of the profiles near ±35 m/s and ±58 m/s manifest the unimodal rainbow feature in the distribution of α_{eff}, which was predicted by Gershnabel and Averbukh [27]. The green solid line in Fig. 3a represents the average of the 21 profiles $\frac{1}{2\times10+1}\sum_{M=-10}^{10} h(v_x; J = 10, M)$, which is the convolution of the two types of rainbow-like singularities. Note that the inner singularities are smeared out owing to the large distribution of their positions. In contrast, the spread

of the positions of the outer singularity forms two broad small peaks in the green profile.

Figure 3b shows $\frac{1}{2J+1}\sum_{M=-J}^{J} h(v_x; J, M)$ for J = 2, 10, and 20. These three J states are selected because, at T = 35 K, the population of the rotational energy levels has its maximum at J = 10, and is close to half of the maximum at J = 2 and 20. Note that the profile for J = 2 is more structured than the other two. Furthermore, the two profiles for J = 10 and 20 are almost identical.

The blue dotted profile in Fig. 3c is $\sum_{J,M} P_J h(v_x; J, M)$ obtained by considering the rotational states up to J = 98. The inner rainbow-like peaks of the profile are smeared out, though the outer ones leave small peaks, as in Fig. 3b. These features also appear in the red line in Fig. 3c, which is the profile of the measured velocity distribution in Fig. 2c. The black dashed line in Fig. 3c depicts $h(v_x; \alpha_{\text{eff}}(T))$, assuming that all the molecules possess the same polarizability $\alpha_{\text{eff}}(T) = \langle\alpha_{\text{eff}}(J, M)\rangle_{J,M}$. This profile is almost identical to the thick gray profile in Fig. 3a – i.e., the profile for $|J = 10, M = \pm 6\rangle$ with $\alpha_{\text{eff}} = 9.8 \times 10^{-40}$ C m^2 V^{-1}. It shows distictive inner sigularities, which clearly disagrees with the experimental result. For these reasons, the state-dependent effective polarizability can be identified as the crucial contribution to the final velocity distribution.

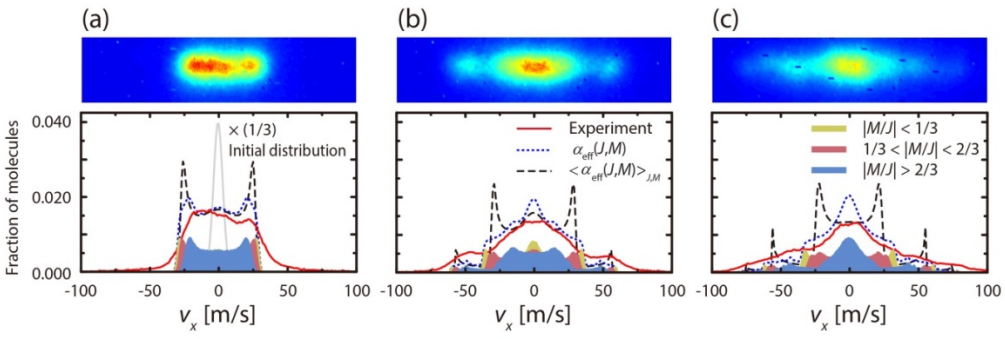

FIG. 4. The three velocity map ion images of CS_2 molecules with the standing wave

of I_0 = (a) 1.0 × 10^{10}, (b) 4.9 × 10^{10}, and (c) 9.8 × 10^{10} W/cm^2 and their profiles along the v_x-axis. The exprimental profiles (red lines) are compared with the simulated ones by using $\alpha_{\mathrm{eff}}(J, M)$ (blue dotted lines) and $<\alpha_{\mathrm{eff}}(J, M)>_{J,M}$ (black dashed lines), as in Fig. 3c.

The velocity distribution of the dispersed molecules in a rotational state varies as the intensity increases. In addition to the increase in the distribution width, the shape changes with the laser intensity. Fig. 4 shows ion images and their velocity profiles (red lines) at I_0 = (a) 1.0, (b) 4.9, and (c) 9.8 × 10^{10} W/cm^2, each of which is compared with two simulated profiles using the state-dependent polarizability $\alpha_{\mathrm{eff}}(J, M)$ (blue dotted lines) and the state-averaged polarizability $<\alpha_{\mathrm{eff}}(J, M)>_{J,M}$ (black dashed lines). As I_0 increases, the velocity of molecules becomes distributed across a wider range (up to about ±80 m/s), and the structure of the distribution varies. The initial velocity profile (× 1/3) is shown in Fig. 4a with a gray line, for comparison. The full series of the ion images and the velocity profiles are shown in Figs. S1 and S2, respectively, in the Supplementary Material [68]. At I_0 = 1.0 × 10^{10} W/cm^2, the experimental profile exhibits a trapezoidal shape. A couple of side peaks appear at I_0 = 2.0 × 10^{10} W/cm^2. The side peaks move outward and become less distinctive as I_0 increses up to 5.9 × 10^{10} W/cm^2; but these peaks disappear when I_0 is further increased. As disccused above, the side peaks are associated with the relatively narrow spread of outer rainbow-like sigularities, as in Fig. 3a. Therefore, the broadening of the spread, due to the increase of I_0, makes the side peaks become less distingushed, and they ultimately disappear.

This variation is well reproduced in the blue simulated profiles using the state-dependent polarizability. On the other hand, similar to the comparison in Fig. 3c, the black profiles simulated using the state-averaged polarizability severely disagree with the red experimental profiles at the parts related to the inner rainbow-like sigularities. The inner singularities are very sharp in the black simulated

profiles, but are smeared out in the red experimental and blue simulated profiles. These comparisons corroborate the fact that the state-dependent effective polarizability should be considered in analyzing the transverse velocity change that results from a pulsed standing wave potential.

Together with other state-of-the-art techniques, such as a pulsed supersonic expansion source [69] and optical standing waves of a tunable velocity [34,58], the state-dependent dispersion is expected to enable state selection of nonpolar molecules. The relative velocity of molecules to the moving standing wave can be made such that only the state of the highest α_{eff} is trapped in the standing wave potential. In this way, the trapped state can be separated from other untrapped states. The detailed scheme of the state selection is described in the Supplementary Material [68]. This new method will nicely complement the techniques for the state selection of polar molecules [70,71]. Especially, this optical technique can be exploited to separate and analyze mixtures of nonpolar conformers, isotopes of homonuclear diatomic molecules, or their spin isomers.

3.4 Conclusions

In conclusion, we observed the rotational state-dependent dispersion of CS_2 molecules by optical standing waves. Simulations using the state-dependent polarizabilities provided better agreement with the experimental observations as compared with simulations based on the average (state-independent) polarizability. This paves the way for selecting a specific state of nonpolar molecules.

3.5 Supplementary materials

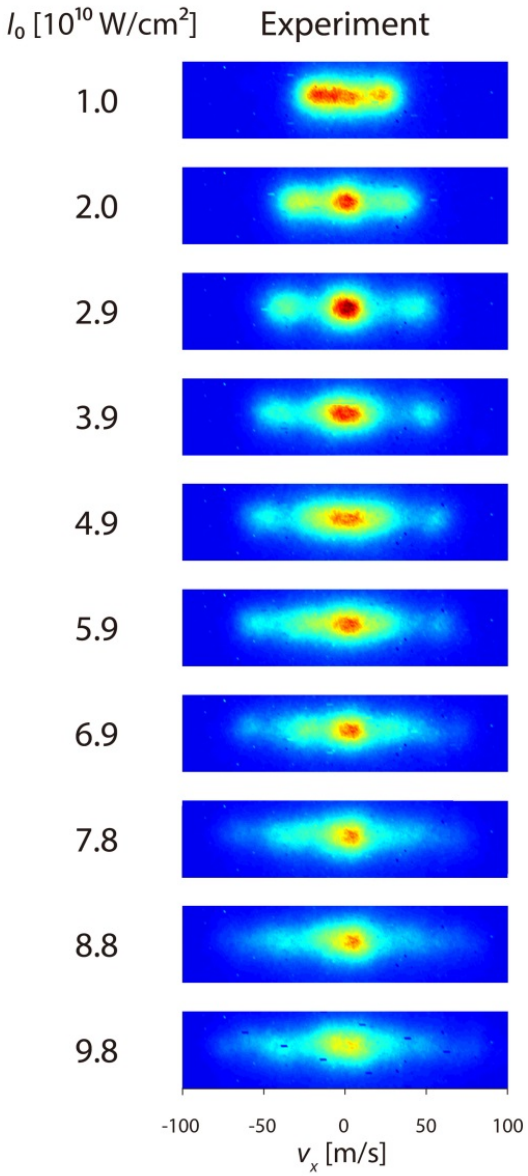

FIG. S1. The ten velocity map ion images of CS_2 molecules observed with standing wave intensities of I_0 = 1.0×10^{10}, 2.0×10^{10}, 2.9×10^{10}, 3.9×10^{10}, 4.9×10^{10}, 5.9×10^{10}, 6.9×10^{10}, 7.8×10^{10}, 8.8×10^{10}, and 9.8×10^{10} W/cm^2.

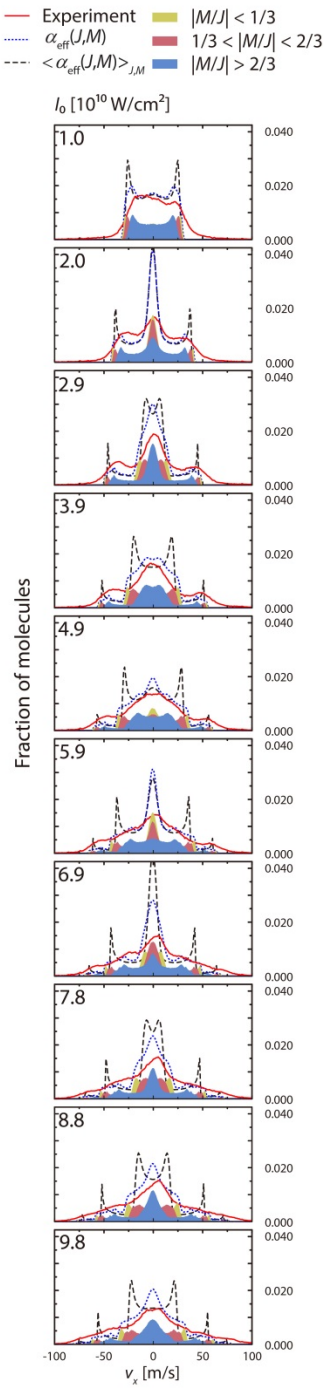

FIG. S2. The ten profiles along the v_x-axis of the images in Fig. S1. The

exprimental profiles (red solid lines) are compared with the simulated ones by using $\alpha_{\mathrm{eff}}(J, M)$ (blue dotted lines) and $<\alpha_{\mathrm{eff}}(J, M)>_{J,M}$ (black dashed lines). The calculated profiles for the three groups of rotational states using $\alpha_{\mathrm{eff}}(J, M)$ are also drawn in each graph.

Figures S1 and S2 show the full series of ion images and velocity profiles, respectively. As the intensity increases from 1.0×10^{10} to 9.8×10^{10} W/cm^2, the velocity of molecules is distributed towards a wider range and the structure of the distribution varies. In Fig. S2 three simulated profiles are added, which pertain to three groups of the rotational states with different ranges of the effective polarizabilities: $\alpha_{\mathrm{eff}} > 10.9 \times 10^{-40}$ C m^2 V^{-1} ($|M/J| < 1/3$); 10.9×10^{-40} C m^2 V^{-1} > $\alpha_{\mathrm{eff}} > 9.2 \times 10^{-40}$ C m^2 V^{-1} ($1/3 < |M/J| < 2/3$); and 9.2×10^{-40} C m^2 V^{-1} > α_{eff} ($|M/J| > 2/3$). At T = 35 K, about one third of the molecules populate the states of each polarizability range. The outmost part of the velocity distribution includes only molecules with large effective polarizabilities, whose angular momenta are aligned perpendicularly to the laser polarization axis. These three groups would be reduced to approximately six rotational states ($|2, \pm2\rangle$, $|2, \pm1\rangle$, $|2, 0\rangle$, $|0, 0\rangle$) if the rotational temperature approaches 0.

Figure S3 shows a phase-space plot, whose horizontal and vertical axes represent the relative x-position (x_{r}) and the relative velocity of molecules ($v_{x,\mathrm{rel}}$) along the x-axis with respect to a moving standing wave, respectively. In Fig. S3a, we draw separatrices for four rotational states, $|0,0\rangle$, $|2,2\rangle$, $|2,1\rangle$, and $|2,0\rangle$. The sizes are different due to the state-dependent polarizability discussed in the main text. Inside of the separatrix for the $|0,0\rangle$ state, for example, the molecules occupying $|0,0\rangle$ are trapped by the standing wave potential. When the molecules in $|0,0\rangle$ are outside of the separatrix, they are not trapped by the potential but their velocity is still influenced by the potential.

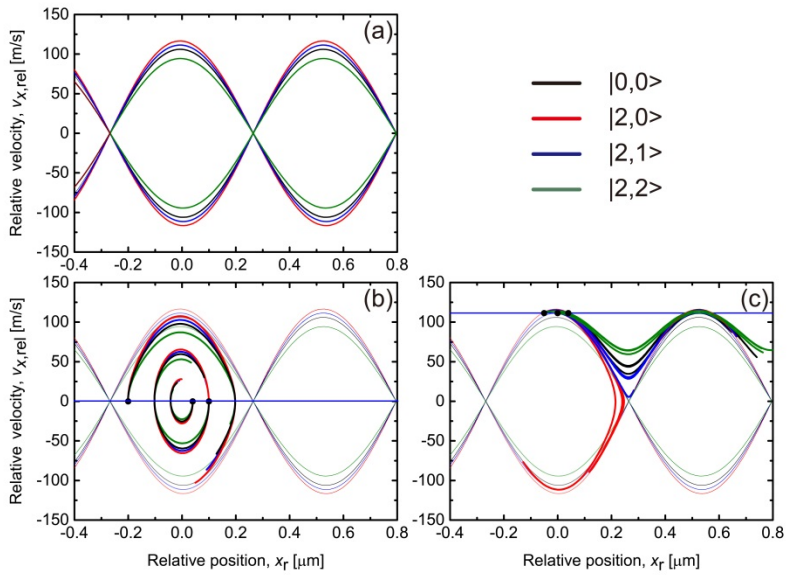

FIG. S3. (a) Separatrices for the four rotational states, |0,0>, |2,2>, |2,1>, and |2,0>, in a phase-space plot. (b) The trapped dynamics of molecules in the four rotational states within a standing wave potential. (c) The trapped and untrapped dynamics of molecules in the |2,0> state and in the other states, respectively, within a moving standing wave of –110 m/s.

First, let us consider the interaction of molecules propagating along the *z*-axis with a standing wave potential propagating along the *x*-axis. If we ignore the transverse velocity spread of the molecules, $v_{x,rel} = 0$ while the standing wave is off. Usually the molecular beam size along the transverse axes (~1 mm) is much larger than the period of the standing wave ($\lambda/2 \sim 0.5$ μm). Then, the blue horizontal line in Fig. S3b depicts the initial condition in the phase space, and all the molecules are trapped in the potential no matter which state they occupy. Curves in Fig. S3b are trajectories of the molecules from selected initial positions in the phase space (black dot) with their color indicating the rotational states of the molecules. In the following simulations we assume a square temporal profile for IR1 and IR2 with

pulse width τ = 12.5 ns and peak intensity I_0 = 9.8 × 10^{10} W/cm^2. During the interaction time τ, when the standing wave potential is on, the molecules rotate clockwise in the phase space, and the degree of the rotation depends on their state-dependent polarizability and the initial position in the phase space. After the interaction time τ, the molecules in the four states are just dispersed over the phase-space area enclosed by the separatrix for each state, namely, the final velocity is distributed with very little state selection.

However, with a moving standing wave, the selection and separation of a quantum state is achievable. When the standing wave is moving at −110 m/s, i.e. $v_{x,\mathrm{rel}}$ = 110 m/s, the initial condition can be illustrated by the horizontal blue line in Fig. S3c. In this condition, only molecules in the |2,0> state can be trapped in the standing wave potential, namely, can be placed inside of the separatrix. Curves in Fig. S3c illustrate trajectories of all four states for the three initial positions. After a proper interaction time, the trapped molecules of |2,0> are decelerated to below −100 m/s, while untrapped molecules of the other states cannot have a negative velocity. Therefore, a moving standing wave can enable the selection of the most polarizable quantum state. The efficiency of the selection can be improved by accelerating a standing wave in a way that its change in velocity is in resonance with the velocity change of the molecules in the target quantum state.

Chapter 4

Fractionation of molecules using a molecule disperser

Abstract

A molecule disperser is constructed using an optical standing wave consisting of two counter-propagating coherent laser beams. A molecule in an optical field undergoes the Stark interaction between the induced molecular dipole moment and the optical field. As a result, the molecular velocity changes owing to the optical force which is given by the negative gradient of the Stark interaction energy. When a beam of a molecular mixture goes through a standing wave, the component molecular species are spatially fractionated because of the differences in velocity changes depending on polarizability-to-mass ratio (PMR) values. As a proof-of-concept demonstration of the molecule disperser, a mixture molecular beam of CS_2 and CH_3I is crossed by a standing wave. Then velocity changes of the molecules dispersed by the standing wave are measured using a velocity map imaging technique.

4.1 Introduction

The optical forces caused by photon-matter interactions are widely used in several fields. Atoms are slowed, cooled, and trapped through transferring the photon linear momenta by absorbing and emitting photons [2]. The control and trapping of microparticles using light [1,7] becomes an important tool in chemistry and chemical biology [5,6]. Using the optical forces, the molecular motion is manipulated e.g., aligning [11], slowing [22,32,56,72], and focusing [20,29,36] molecules. The optical forces were used in separation science [6,73]. When a microparticle solution flows against the direction of a focused laser beam propagation, the particles are separated by the size [74] and refractive index [75]. In this method, the optical force acts against the drag force of a liquid flow. Such an optical force was also used to propel suspended particles to migrate with different mobilities along the laser propagation direction according to the particle size [76,77]. A slightly different scheme of an optical separation method is laser light propagation perpendicular to a particle flow, which enables different particle traveling along different trajectories [78,79].

Separation of molecules in a molecular beam plays an important role in molecular physics. It can be performed using such devices as a Stark deflector or hexapole focuser, which utilize the interaction of the molecular permanent dipole moment with an inhomogeneous electric field. These methods were used for the separation of structural isomers [71,80], clusters [81], and molecules at different quantum states [82] or different nuclear spin states [83] with respect to the effective dipole moment-to-mass ratios. These researches enabled further important studies such as quantum-state resolved collision dynamics [84] or state dependent degree of alignment or orientation of molecules [85]. On the other hand, a molecule prism separating small molecules in a molecular beam was demonstrated [21]. It utilized the nonresonant dipole force whose magnitude is proportional to the polarizability of the molecules. Since all molecules are polarizable, this optical dipole force method is applicable to all molecules including nonpolar molecules, which are hard

to handle using static field methods. Some interesting optical separation cases, such as the separation of isotopes $^{28}N_2$ and $^{30}N_2$, equal-mass molecules, e.g., $^{28}N_2$ and CO [86], or same molecules at different quantum states [50], were also suggested. In general, pulsed laser beams of extremely high peak intensities in a range of 10^{11}–10^{12} W/cm^2 were used in optical dipole force experiments because of a relatively smaller Stark interaction energy between an electric field and the induced dipole moment than that between an electric field and a permanent dipole. Thus, only noncontinuous separations were achieved by the optical method. Furthermore, optical separation of conformers or same molecules at different quantum states has not been achieved experimentally.

In this work, a new separation scheme is introduced. We employ an optical standing wave that is composed of two counter-propagating coherent laser beams instead of a single focused laser beam to separate CS_2 and CH_3I molecules which have different polarizability-to-mass ratios (PMRs) values. The standing wave was suggested to reflect low-energy molecules [53], and moving standing waves were used to decelerate molecules[32,72] and accelerate [34] neutral particles. In our case, the standing wave lies perpendicular to a molecular beam to act as a molecule disperser [24]. Since the maximum field gradient along the laser beam axis is much stronger than that along the radial direction, and the optical dipole force is proportional to the field gradient, the maximum optical dipole force from the standing wave is much larger than that from a single focused Gaussian beam. The deflection efficiency, which is defined as the maximum velocity change divided by the maximum laser intensity, was enhanced by more than 10 times, in comparison to the case of a molecule lens [20], where CS_2 molecules were deflected using a single focused laser beam.

4.2 Experimental

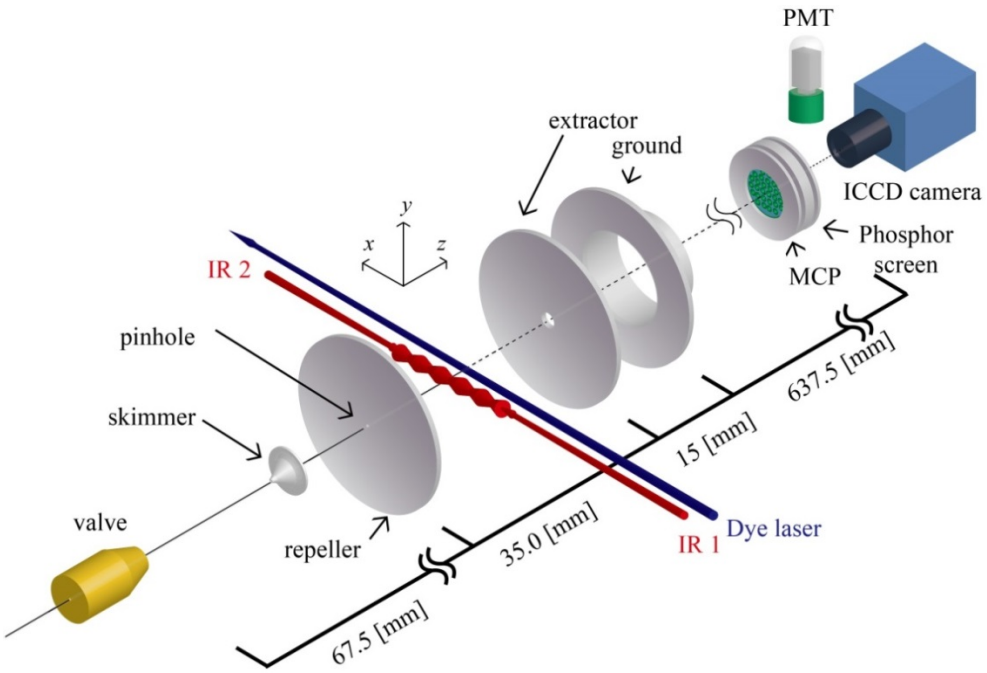

FIG. 1. Schematics of the experimental setup. A mixture molecular beam moving along the *z*-axis is dispersed by a standing wave, which consists of two counter-propagating infrared laser beams IR1 and IR2.

Figure 1 shows the schematics of the experimental setup used for molecular fractionation. A molecular beam was produced using the supersonic expansion of a mixture of 64 Torr CS_2 and 86 Torr CH_3I vapors seeded in an Ar buffer gas held at 2 atm through a pulsed solenoid valve operating at a frequency of 10 Hz. The molecular beam was collimated by a skimmer and then entered a detection chamber through a a pinhole with a diameter of 0.6 mm. The *y*-axis and *z*-axis in this system were defined as the vertical and molecular beam directions, respectively. The pressure inside the detection chamber was maintained at approximately 6×10^{-7} Torr. Two windows at each side of the detection chamber enabled two laser beams from both sides to enter the detection chamber. An infrared (IR) beam pulse from an Nd:YAG laser (wavelength of 1064 nm, Powerlite 8000,

Continuum, Santa Clara, CA, USA), which had a pulse duration of 12.5 ns, was divided into two beams using a beam splitter, and each beam was linearly polarized along the *y*-axis using a Glan-laser polarizer (Newport, Irvine, CA, USA). Before entering the detection chamber, each beam was focused using convex lenses with focal lengths of 17.5 cm and 20 cm placed at the front and back of the chamber, respectively. The waist radii of the focused front and back beams were 18 μm and 22 μm, respectively. The two counter-propagating focused IR laser beams were overlapped at the center of the detection chamber to form a pulsed standing wave. The center of the IR laser focus was chosen as the origin point. Molecules were dispersed by the pulsed standing wave and then ionized by a focused 7 ns dye laser beam (wavelength of 455.650 nm, ND6000, Continuum) pumped by the third harmonics of an Nd:YAG laser (wavelength of 355 nm, Surelite II-10, Continuum, Santa Clara, CA, USA) through a multiphoton ionization process. The velocities of molecular ions were analyzed using a velocity map imaging (VMI) technique [38]. By adjusting the voltage of three electrodes: repeller, extractor, and ground, we could focus ions with the same velocity at the same position of a 2D ion detector. The voltage combination of the electrodes used for VMI was 900, 610, and 0 V for repeller, extractor, and ground, respectively. The 2D ion detector was composed of a microchannel plate (MCP) and a phosphor screen. The times of flight (TOF) were 13.78 μs and 18.98 μs for CS_2^+ and CH_3I^+ ions, respectively. They were measured by analyzing photomultiplier tube (PMT) signals on an oscilloscope. The ion images of each species on the phosphor screen were recorded individually using a gated ICCD camera (DH534-18F-04, Andor, Belfast, UK).

4.3 Results and Discussion

The Stark potential of a molecule in a standing wave is $U(x,t) = -\frac{1}{2}\alpha\eta I_0 \exp[-2(v_z t)^2/\omega_0^2]\exp[4\ln 2t^2/\tau^2]\cos^2(2\pi x/\lambda)$, where α and η are the polarizability of the molecule and the vacuum impedance, respectively, and I_0 is

the peak intensity of the standing wave. v_z = 521 m/s is the molecular beam velocity and $v_z t = z$ is the z-coordinate of the molecule at time t. τ and λ are the pulse duration and wavelength of the both counter-propagating beams, respectively. When molecules go through such a time dependent potential, the motions of the molecules are to be described using the time dependent Schrödinger equation. However, the trajectories of the molecules could be calculated by classical mechanics in such systems [53]. The maximum force along the z-axis $\nabla_z U(x,t)(\propto \nabla_z \exp\left[-2z^2/\omega_0^2\right])$ is several ten times smaller than that along the x-axis, which is $\nabla_x U(x,t)(\propto \nabla_x \cos^2\left(2\pi x/\lambda\right))$. Thus, we consider only the x-directional optical force to describe the molecular dispersion. Velocity changes of the molecules deflected by the standing wave can be calculated by $\Delta v = -\frac{1}{m}\int_{-\infty}^{\infty} \nabla U_x(x,t)dt$.

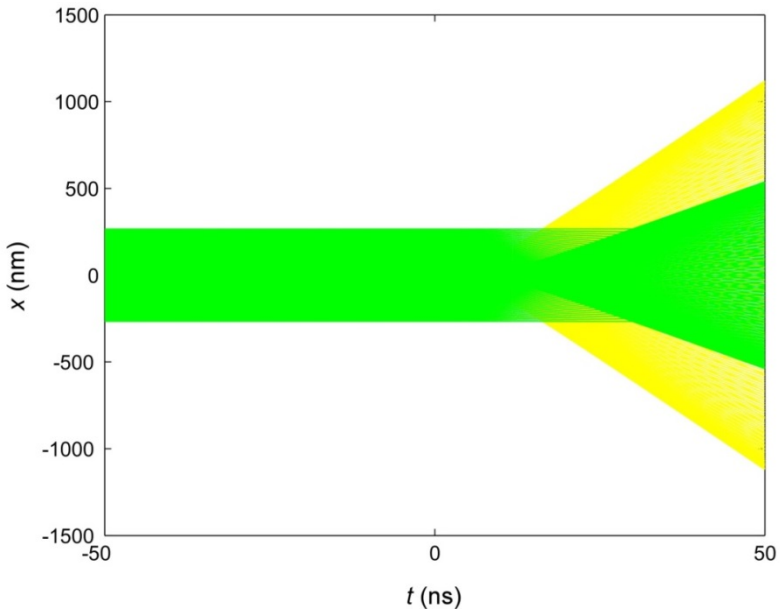

FIG. 2. Simulated trajectories of CS_2 (yellow) and CH_3I (green) molecules in a

range of [–266, 266] nm in the *xz* plane under the standing wave of $I_0 = 4 \times 10^{10}$ W/cm^2.

Figure 2 shows the simulated trajectories of both CS_2 (yellow) and CH_3I (green) molecules with respect to different initial *x*-positions under the influence of the *x*-directional optical force from –50 ns to 50 ns using the Verlet algorithm [87]. The peak intensity I_0 of the standing wave was 4×10^{10} W/cm^2 and the polarizability of CS_2 and CH_3I used in this simulation were 9.6×10^{-40} Cm^{2}V^{-1} [20] and 8.4×10^{-40} Cm^{2}V^{-1} [88], respectively. The initial velocities of the molecules along the *x*-axis and *z*-axis were 0 and 521 m/s, respectively. The standing wave potential was a series of the potential wells that have a period of $\lambda/2$. We just show the molecules passing through one potential well. We can easily see in Fig. 2 that the degree of dispersion of CS_2 molecules by the standing wave potential is larger than that of CH_3I molecules. This implies that CS_2 molecules should be dispersed wider than CH_3I molecules by the pulsed standing wave.

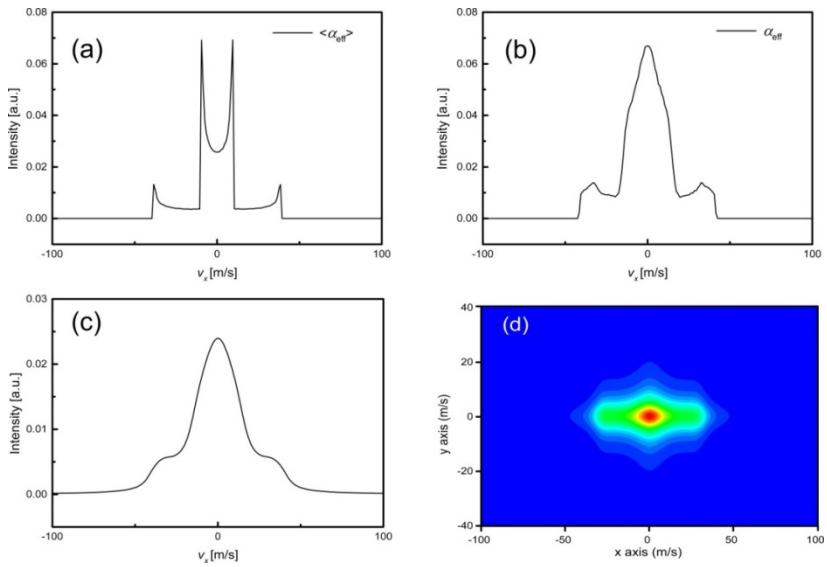

FIG. 3. (a) Final velocity distribution profile $g(v_x)$ with the average polarizability and an initial velocity distribution of the molecules in the *x*- and *z*- directions is zero. (b) $g(v_x)$ of the initial velocity distribution of the molecules in the *x*- and *z*-directions is 8.3 m/s and 44 m/s, respectively, and the effective polarizability values with respect to different rotational states are used. (c) The same plot as for (b) but a blurring effect of the 2D detector is convoluted. (d) The expected velocity map image obtained using the simulation.

Figure 3 shows the final velocity distribution profiles. Figure 3(a) depicts a Monte Carlo simulated final velocity distribution profile $g(v_x)$ of CS_2 molecules under the same conditions as in the simulation, the results of which are demonstrated in Fig. 2, except for the initial *x*-position, which was ranged from –300 μm to 300 μm. The number of molecules with their final velocities in a small range of $[v_x - \delta v_x, v_x + \delta v_x]$ was plotted with respect to the final velocity v_x. We can see the rainbow structures at $v_x = \pm 29$ m/s. The individual effective polarizability value corresponding to the rotational state of each molecule must be used instead of the mean value, which was not considered above. Owing to the polarizability anisotropy, the effective polarizability α_{eff} is $\alpha_{\text{eff}} = [(\alpha_{\parallel} - \alpha_{\perp})A + \alpha_{\perp}]$, where $\alpha_{\parallel}$ and $\alpha_{\perp}$ are polarizabilities along and perpendicular to the molecular axis, respectively. $A = \overline{\cos^2 \theta}$ is the averaged cosine square value of angle θ between the molecular axis and the laser polarization axis. The distribution function $f(A)$ was introduced in reference [28]. In the thermal case, $f(A)$ is given by

$$f(A) = \frac{1}{\sqrt{1-2A}}. \tag{1}$$

This function obtained from the classical mechanical argument is used to determine the distribution of the effective polarizability values. Linear molecules, such as CS_2,

rotate in the plane perpendicular to the total angular momentum. A different rotating plane results in different *A*. While considering an isotropic distribution of the angular momentum directions, one can get the above distribution function *f*(*A*). The analogy of quantum mechanical and classical mechanical arguments of *f*(*A*) is shown in reference [27]. Thus, we use *f*(*A*) through classical mechanics only when simulating final velocity distribution function $g(v_x)$. The initial velocity spread along the *x*-axis and *z*-axis also must be considered. In Fig. 3(b), the initial velocity distribution of the molecular beam was 8.3 m/s (through analyzing Fig. 4 (a)) and 44 m/s [42] full width at half maximum (FWHM) of the Gaussian distribution along the *x*-axis and *z*-axis, respectively. The effective polarizability values were used to estimate the final velocity distribution $g(v_x)$ along the *x*-axis. We can see that the rainbow structures near $v_x = \pm 29$ m/s are blurred. Figure 3(c) is the convolution result of velocity distribution $g(v_x)$ in Fig. 3(b) and a blurring effect of our 2D detector. The blurring effect of the 2D detector was measured by analyzing single-ion spot images, which gave width values of 8.7 m/s and 7.8 m/s along the *x*-axis and *y*-axis, respectively, when fitted to the Lorentzian function. Figure 3(c) represents the expected velocity distribution along the *x*-axis, which is obtained using the 2D detector. Figure 3(d) is the expected velocity map image with the parameters introduced above, while considering the velocity distribution along the *y*-axis.

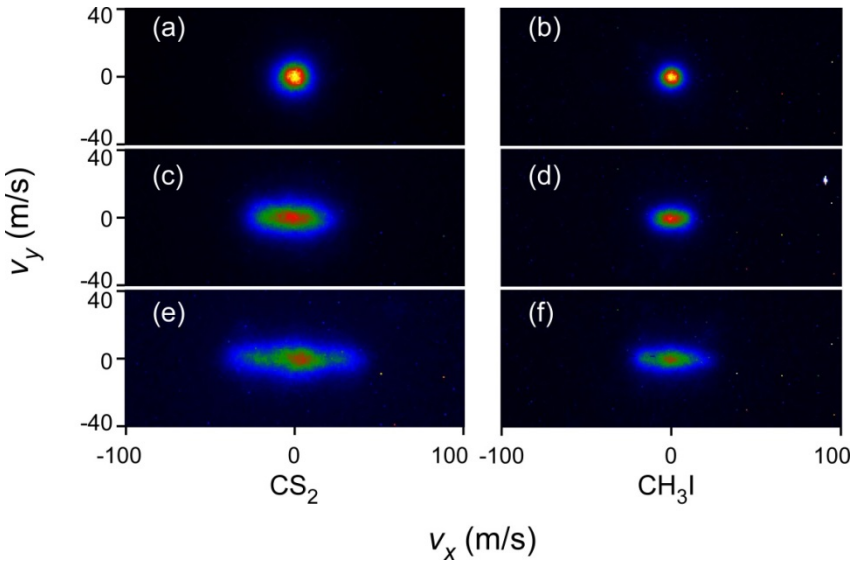

FIG. 4. (a), (c), and (e) Velocity map images of CS_2 molecular ions recorded by the ICCD camera gated at 13.78 ± 1 μs. (b), (d), and (f) Those of CH_3I gated at 18.98 ± 1 μs. (a) and (b) The case of standing wave off. (b) and (d) The case of $I_0 = 4 \times 10^{10}$ W/cm^2. (e) and (f) The case of $I_0 = 8 \times 10^{10}$ W/cm^2.

Symmetric-top molecules, such as CH_3I, behave in a complicated torque free classical motion. Compared with linear molecules that rotate in a plane, the rotation of symmetric-top molecules is not restricted by a plane. The distribution function $f(A)$ for symmetric-top molecules was introduced in reference [28]. We repeated the simulation process introduced in this report in order to apply $f(A)$ to further study of CH_3I molecule dispersion. The experimental velocity map images are shown in Fig. 4. The CS_2 images in the first column were recorded in a TOF range of 13.78 ± 1 μs and the CH_3I images in the second column were recorded in a TOF range of 18.98 ± 1 μs. Such velocity space images were obtained from transformation of the original image, which was recorded using the ICCD camera, scaled by the TOF of each molecular species, since the displacement of an original

image spot is equal to the TOF multiplied by velocities along the *x*- and *y*-directions. Figures 4(a) and 4(b) depict cases of standing wave off; Figs. 4(c) and 4(d) were obtained with a standing wave of peak intensity $I_0 = 4 \times 10^{10}$ W/cm^2, and Figs. 4(e) and 4(f) were obtained with $I_0 = 8 \times 10^{10}$ W/cm^2. The experimental image shown in Fig. 4(c) is consistent with the simulated image shown in Fig. 3(d), which means that the experimental data were consistent with the theory of optical deflection. Figure 5(a) is the comparison result of the velocity distribution of CS_2 and CH_3I molecules from the simulation, which was performed using the process mentioned in Fig. 3(b). The velocity profile obtained from Figs. 4(e) and 4(f) are shown in Fig. 5(b). We can see that the velocity distribution of CS_2 ions in Fig. 5(b) is wider than that of CH_3I ions. However, these profiles contain the blurring effects from the 2D detector and from an electron recoil process, which are difficult to determine in this study. Thus, we compared the simulation results in Fig. 5(a), which can be considered as deconvolution of the blurring effect from the experimental images. We think that the mismatch of the experimental and theoretical results is caused by several blurring effects. We can see from Fig. 5(a) that the final velocities of CH_3I molecules do not exceed 39 m/s while that of CS_2 molecules can reach 49 m/s. Hence, the dispersion angles of CH_3I and CS_2 molecules are 2.9° and 3.9°, respectively. One can obtain CS_2 molecules in a range from 2.9° to 3.9°.

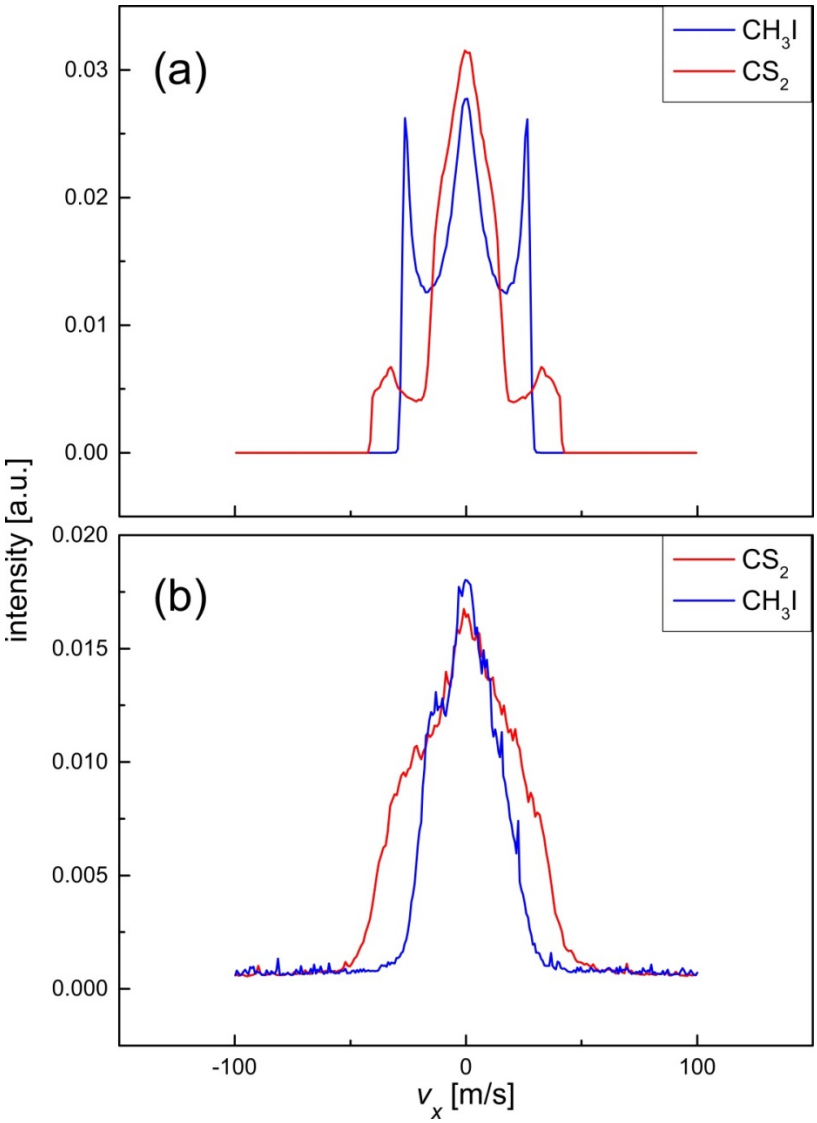

FIG. 5 (a) Simulated velocity map image profiles of CS_2 and CH_3I molecules. (b) Velocity map image profiles from the images shown in Figs. 4(e) and 4(f).

4.4 Conclusions

In this work, we have shown different degrees of molecule dispersion according to different PMR values of the molecules in a mixture molecular beam

were obtained by employing a standing wave that acts as a molecule disperser. The simulated images were consistent with the experimental images. Both simulation and experimental data show that CS_2 molecules were dispersed more widely than CH_3I molecules. This fractionation method is expected to be usable for not only different molecular species but also isotopes, isomers, or conformers as long as two species have different PMR ratios.

References

[1] A. Ashkin, Phys. Rev. Lett. **24**, 156 (1970).
[2] W. D. Phillips, Rev. Mod. Phys. **70**, 721 (1998).
[3] C. Adams and E. Riis, PROG. QUANT. ELECTRON. **21**, 1 (1997).
[4] W. Ketterle, Rev. Mod. Phys **74**, 1131 (2002).
[5] A. Ashkin, Proc. Natl. Acad. Sci **94**, 4853 (1997).
[6] A. Jonáš and P. Zemanek, Electrophoresis **29**, 4813 (2008).
[7] A. Ashkin, J. Dziedzic, J. Bjorkholm, and S. Chu, Opt. Lett. **11**, 288 (1986).
[8] R. L. Eriksen, P. J. Rodrigo, V. R. Daria, and J. Glückstad, Appl. Opt **42**, 5107 (2003).
[9] S. L. Neale, M. P. MacDonald, K. Dholakia, and T. F. Krauss, Nature Mater. **4**, 530 (2005).
[10] P. Galajda and P. Ormos, Opt. Express **11**, 446 (2003).
[11] H. Stapelfeldt and T. Seideman, Rev. Mod. Phys. **75**, 543 (2003).
[12] E. S. Shuman, J. F. Barry, D. R. Glenn, and D. DeMille, Phys. Rev. Lett. **103**, 223001 (2009).
[13] J. F. Barry, E. S. Shuman, E. B. Norrgard, and D. DeMille, Phys. Rev. Lett. **108**, 103002 (2012).
[14] J. Barry, D. McCarron, E. Norrgard, M. Steinecker, and D. DeMille, Nature **512**, 286 (2014).
[15] E. Shuman, J. Barry, and D. DeMille, Nature **467**, 820 (2010).
[16] M. Yeo, M. T. Hummon, A. L. Collopy, B. Yan, B. Hemmerling, E. Chae, J. M. Doyle, and J. Ye, Phys. Rev. Lett. **114**, 223003 (2015).
[17] H. Stapelfeldt, H. Sakai, E. Constant, and P. B. Corkum, Phys. Rev. Lett. **79**, 2787 (1997).
[18] B. Friedrich and D. Herschbach, Phys. Rev. Lett. **74**, 4623 (1995).
[19] T. Seideman, Phys. Rev. A **56**, R17 (1997).
[20] B. S. Zhao *et al.*, Phys. Rev. Lett. **85**, 2705 (2000).
[21] B. S. Zhao, S. H. Lee, H. S. Chung, S. Hwang, W. K. Kang, B. Friedrich, and D. S. Chung, J. Chem. Phys **119**, 8905 (2003).
[22] R. Fulton, A. I. Bishop, and P. Barker, Phys. Rev. Lett. **93**, 243004 (2004).
[23] X. N. Sun, S. E. Shin, B. S. Zhao, and D. S. Chung, Front. Phys. **2** (2014).
[24] X. N. Sun, L. Y. Kim, B. S. Zhao, and D. S. Chung, Phys. Rev. Lett. **115**, 223001 (2015).
[25] M. Artamonov and T. Seideman, Nano Lett. **10**, 4908 (2010).
[26] E. Gershnabel and I. S. Averbukh, Phys. Rev. Lett. **104**, 153001 (2010).
[27] E. Gershnabel and I. S. Averbukh, Phys. Rev. A **82**, 033401 (2010).
[28] E. Gershnabel and I. S. Averbukh, J. Chem. Phys. **135**, 084307 (2011).
[29] S. M. Purcell and P. F. Barker, Phys. Rev. Lett. **103**, 153001 (2009).
[30] M. Lemeshko, R. V. Krems, J. M. Doyle, and S. Kais, Mol. Phys. **111**, 1648 (2013).
[31] T. Seideman, J. Chem. Phys. **111**, 4397 (1999).
[32] R. Fulton, A. Bishop, M. Shneider, and P. Barker, Nat. Phys. **2**, 465 (2006).
[33] A. I. Bishop, L. Wang, and P. F. Barker, New J. Phys. **12**, 073028 (2010).

[34] C. Maher-McWilliams, P. Douglas, and P. F. Barker, Nature Photon. **6**, 386 (2012).
[35] C. Schröter, K. Kosma, and T. Schultz, Science **333**, 1011 (2011).
[36] H. S. Chung, B. S. Zhao, S. H. Lee, S. Hwang, K. Cho, S.-H. Shim, S.-M. Lim, W. K. Kang, and D. S. Chung, J. Chem. Phys. **114**, 8293 (2001).
[37] S. Couris, E. Patsilinakou, M. Lotz, E. R. Grant, C. Fotakis, C. Cossart-Magos, and M. Horani, J. Chem. Phys. **100**, 3514 (1994).
[38] A. T. J. B. Eppink and D. H. Parker, Rev. Sci. Instrum. **68**, 3477 (1997).
[39] H. Stapelfeldt, H. Sakai, E. Constant, and P. Corkum, Phys Rev Lett. **79**, 2787 (1997).
[40] B. S. Zhao *et al.*, Phys. Rev. Lett **85**, 2705 (2000).
[41] B. E. A. Saleh and M. C. Teich, *Fundamentals of Photonics* (John Wiley & Sons, Inc. , New York, 1991).
[42] S. M. Purcell, Ph. D. thesis, University College London, 2010.
[43] B. Friedrich and D. Herschbach, J. Chem. Phys. **111**, 6157 (1999).
[44] B. Friedrich and D. Herschbach, J. Phy. Chem. A **103**, 10280 (1999).
[45] L. Cai, J. Marango, and B. Friedrich, Physical Review Letters **86**, 775 (2001).
[46] H. Sakai, S. Minemoto, H. Nanjo, H. Tanji, and T. Suzuki, Phys. Rev. Lett. **90**, 083001 (2003).
[47] M. Härtelt and B. Friedrich, J. Chem. Phys. **128**, 224313 (2008).
[48] J. H. Nielsen, H. Stapelfeldt, J. Küpper, B. Friedrich, J. J. Omiste, and R. González-Férez, Phys. Rev. Lett. **108**, 193001 (2012).
[49] T. Seideman, J. Chem. Phys. **106**, 2881 (1997).
[50] T. Seideman, J. Chem. Phys. **107**, 10420 (1997).
[51] B. Friedrich, Physical Review A **61**, 025403 (2000).
[52] S. M. Purcell and P. F. Barker, Phys. Rev. A **82**, 033433 (2010).
[53] P. Ryytty and M. Kaivola, Phys. Rev. Lett. **84**, 5074 (2000).
[54] P. Barker and M. Shneider, Phys. Rev. A **64**, 033408 (2001).
[55] P. Barker and M. Shneider, Phys. Rev. A **66**, 065402 (2002).
[56] G. Dong, W. Lu, and P. F. Barker, Phys. Rev. A **69**, 013409 (2004).
[57] J. Ramirez-Serrano, K. E. Strecker, and D. W. Chandler, Phys. Chem. Chem. Phys. **8**, 2985 (2006).
[58] R. Fulton, A. I. Bishop, M. N. Shneider, and P. F. Barker, Nat. Phys. **2**, 465 (2006).
[59] E. Gershnabel and I. S. Averbukh, J. Chem. Phys. **134**, 054304 (2011).
[60] E. Gershnabel, M. Shapiro, and I. S. Averbukh, J. Chem. Phys. **135**, 194310 (2011).
[61] S. Fleischer, I. S. Averbukh, and Y. Prior, Phys. Rev. lett. **99**, 093002 (2007).
[62] J. O. Hirschfelder, C. F. Curtiss, and R. B. Bird, *Molecular Theory of Gases and Liquids* (Wiley, New York, 1954).
[63] R. Velotta, N. Hay, M. B. Mason, M. Castillejo, and J. P. Marangos, Phys. Rev. Lett **87**, 183901 (2001).
[64] G. Scoles, D. Bassi, U. Buck, and U. Valbusa, *Atomic and Molecular Beam*

Methods (Oxford University Press, New York, 1988).
[65] S. M. Purcell, Ph. D. thesis, University College London, 2010.
[66] R. Torres, R. de Nalda, and J. P. Marangos, Physical Review A **72**, 023420 (2005).
[67] P. Atkins and J. de Paula, *Atkins' Physical Chemistry* (Oxford University Press, New York, 2014), 9th edn.
[68] See Supplemental Material at [URL will be inserted by publisher] for the full series of the ion images, the velocity profiles, and the detailed scheme of the state selection.
[69] M. Hillenkamp, S. Keinan, and U. Even, Journal of Chemical Physics **118**, 8699 (2003).
[70] S. Y. T. van de Meerakker, H. L. Bethlem, and G. Meijer, Nat. Phys. **4**, 595 (2008).
[71] F. Filsinger, J. Küpper, G. Meijer, J. L. Hansen, J. Maurer, J. H. Nielsen, L. Holmegaard, and H. Stapelfeldt, Angew. Chem. Int. Ed. **48**, 6900 (2009).
[72] R. Fulton, A. Bishop, M. Shneider, and P. Barker, J. Phys. B **39**, S1097 (2006).
[73] B. S. Zhao, Y.-M. Koo, and D. S. Chung, Anal. Chim. Acta **556**, 97 (2006).
[74] T. Kaneta, Y. Ishidzu, N. Mishima, and T. Imasaka, Analytical chemistry **69**, 2701 (1997).
[75] S. J. Hart and A. V. Terray, Applied physics letters **83**, 5316 (2003).
[76] A. Hirai, H. Monjushiro, and H. Watarai, Langmuir **12**, 5570 (1996).
[77] H. Monjushiro, A. Hirai, and H. Watarai, Langmuir **16**, 8539 (2000).
[78] S. B. Kim, S. Y. Yoon, H. J. Sung, and S. S. Kim, Analytical chemistry **80**, 6023 (2008).
[79] S. J. Staton, S. Y. Kim, S. J. Hart, G. E. Collins, and A. Terray, Analytical chemistry **85**, 8647 (2013).
[80] F. Filsinger, U. Erlekam, G. von Helden, J. Küpper, and G. Meijer, Phys. Rev. Lett. **100**, 133003 (2008).
[81] S. Trippel, Y.-P. Chang, S. Stern, T. Mullins, L. Holmegaard, and J. Küpper, Physical Review A **86**, 033202 (2012).
[82] T. D. Hain, R. M. Moision, and T. J. Curtiss, J. Chem. Phys **111**, 6797 (1999).
[83] D. A. Horke, Y.-P. Chang, K. Długołęcki, and J. Küpper, Angew. Chem. Int. Ed. **53**, 11965 (2014).
[84] M. Kirste *et al.*, Science **338**, 1060 (2012).
[85] L. Holmegaard, J. H. Nielsen, I. Nevo, H. Stapelfeldt, F. Filsinger, J. Küpper, and G. Meijer, Phys. Rev. Lett. **102**, 023001 (2009).
[86] G. Dong, W. Lu, and P. Barker, J. Chem. Phys. **118**, 1729 (2003).
[87] J. E. Hasbun, *Classical Mechanics with MATLAB Applications* (Jones and Bartlett, 2009).
[88] A. Sugita, M. Mashino, M. Kawasaki, Y. Matsumi, R. J. Gordon, and R. Bersohn, J. Chem. Phys **112**, 2164 (2000).